Correcting the AMSR-E NASA Soil Moisture for the Effects of Vegetation Transmittance and Emission: A Refined 2002–2011 Dataset

Qiuxia Xie, Li Jia, *Member, IEEE*, Massimo Menenti, and Qiting Chen

***Abstract*—The Advanced Microwave Scanning Radiometer-Earth Observing System/National Aeronautics and Space Administration (AMSR-E/NASA) daily global soil moisture (SM) product (2002–2011, 25-km resolution) has been widely used but exhibits limited sensitivity to intra-annual and interannual variability in many regions. This limitation is mainly attributed to inaccurate parameter values (A_0 and A_1), which account for vegetation transmittance and emission in the AMSR-E/NASA SM retrieval algorithm. To address this issue, we recalibrated A_0 and A_1 using in situ SM measurements from 13 observation networks (192 sites) and established their empirical relationships with fractional vegetation cover (FVC). Four dominant land cover types (i.e., bare soil, grassland, cropland, and forest) were considered due to their global representativeness and extensive coverage with in situ SM measurements. Based on these relationships, we generated global maps of A_0 and A_1 and produced an improved Global Daily AMSR-E SM dataset (GD_AMSR-E_SM; 2002–2011, 25-km resolution) using the Global Land Surface Satellite (GLASS) FVC dataset and AMSR-E observations. Validation against in situ SM measurements within six independent networks shows that the GD_AMSR-E_SM dataset achieves greater consistency with in situ SM measurements, with mean absolute error (MAE) and root-mean-square error (RMSE) values of 0.026 and 0.032 cm^3/cm^3, respectively. This represents average reductions of 20% and 26% compared with the AMSR-E/NASA, AMSR-E/Japan Aerospace Exploration Agency (JAXA), and AMSR-E/Land Parameter Retrieval Model (LPRM) SM products. The enhanced algorithm improves the accuracy and reliability of AMSR-E observations for long-term global SM monitoring.**

***Index Terms*—Advanced Microwave Scanning Radiometer-Earth Observing System (AMSR-E), National Aeronautics and Space Administration (NASA), soil moisture (SM), vegetation transmittance and emission.**

I. Introduction

SOIL moisture (SM) is one of the indispensable components of the land surface water circulation system, and it is also one of the key factors determining the exchange of energy and moisture between the atmosphere and the land surface [1]. With the continuous development of remote sensing technology, the use of remote sensing measurements to monitor SM quickly and efficiently has become common [2]. At present, three types of remote sensing signals are used: visible and near-infrared reflectance, thermal infrared emittance, and microwave backscatter and emittance [3]. SM affects the spectral properties of the soil by influencing the reflectance of the soil. Visible and near-infrared reflectance is highly sensitive to soil water content and can be used to retrieve SM [4]. However, visible–near-infrared observation is severely affected by clouds, rain, and other atmospheric effects, making it difficult to achieve a good spatial and temporal coverage of SM retrievals. Compared with thermal infrared and optical remote sensing, microwave remote sensing has the unique advantage of all-sky retrievals. There are two main advantages: 1) microwave radiation has a good transmittance through moderately dense vegetated surfaces and high sensitivity to SM and 2) microwave is less affected by atmospheric factors such as clouds and rain, and all-sky observations are feasible. These advantages make microwave remote sensing the primary method for retrieving global SM, which is widely documented in the literature [5], [6], [7].

Many satellites equipped with active/passive microwave sensors have been successfully launched since the 1970s (see Table I) [8], [9]. Among them, the Advanced Microwave Scanning Radiometer-Earth Observing System (AMSR-E) is a passive microwave radiometer aboard the Aqua satellite jointly developed by the National Aeronautics and Space Administration (NASA) and Japan Aerospace Exploration Agency (JAXA). AMSR-E achieves global coverage with ascending and descending orbits (except for a few polar regions) in two days [10], [11]. Unlike the microwave radiometers onboard satellite missions such as the Soil Moisture and Ocean Salinity (SMOS) and Soil Moisture Active Passive (SMAP), AMSR-E measures emittance over a wide frequency range

Received 18 March 2025; revised 19 August 2025 and 23 October 2025; accepted 7 November 2025. Date of publication 13 November 2025; date of current version 1 December 2025. This work was supported in part by the Natural Science Foundation of Shandong Province under Grant ZR2022QD138, in part by the Natural Science Foundation under Grant 42301367 and Grant 42090014, in part by the Open Fund of the State Key Laboratory of Remote Sensing Science under Grant OFSLRSS202326, in part by Chinese Academy of Sciences President's International Fellowship Initiative under Grant 2020VTA0001 and Grant 2025PVA0200, and in part by the Most High Level Foreign Expert Program under Grant G2022055010L. *(Corresponding author: Li Jia.)*

Qiuxia Xie is with the School of Surveying and Geo-Informatics, Shandong Jianzhu University, Jinan 250101, China (e-mail: xieqiuxia21@sdjzu.edu.cn).

Li Jia and Qiting Chen are with the State Key Laboratory of Remote Sensing and Digital Earth, Aerospace Information Research Institute, Chinese Academy of Sciences, Beijing 100101, China (e-mail: jiali@aircas.ac.cn).

Massimo Menenti is with the State Key Laboratory of Remote Sensing and Digital Earth, Aerospace Information Research Institute, Chinese Academy of Sciences, Beijing 100101, China, also with Delft University of Technology, 2600 AA Delft, The Netherlands, and also with the Institute of Tibetan Plateau Research, Chinese Academy of Sciences, Beijing 100094, China.

This article has supplementary downloadable material available at https://doi.org/10.1109/TGRS.2025.3632239, provided by the authors.

Digital Object Identifier 10.1109/TGRS.2025.3632239

TABLE I
OVERVIEW OF MAJOR SATELLITE ACTIVE/PASSIVE MICROWAVE SENSORS

Properties	Satellites	Sensors	Frequency Coverage (GHz)	Band number	Polarization mode	Temporal coverage (year)	Ob. Time	Temporal resolution	Spatial resolution	Spatial coverage	MR
Passive microwave	Aqua	AMSR-E	6.9~89	6	V, H	2002~2011	01:30; 13:30	1~2 days	5~56km	Global	[11]
	Coriolis	WindSat	6.8~37	5	V, H	2003~2012	06:00; 18:00	1 day	13~60km	60N~60S	[20]
	GCOM-W	AMSR-2	6.9~89	14	V, H	2012~now	01:30; 13:30	1~2 days	5~62km	Global	[21]
	FY3-B	MWRI	10.65~89	10	V, H	2011~2020	01:40; 13:40	1 day	15~85km	Global	[22]
	FY3-C	MWRI	10.65~89	10	V, H	2014~ now	10:40; 22:40	1 day	15~85km	Global	[22]
	SMOS	MIRAS	1.4	1	V, H, VH, HV	2010~now	06:00; 18:00	3 days	35~50km	Global	[23]
	SMAP	SMAP	1.41	1	V, H	2015~now	06:00; 18:00	2~3days	40km	Global	[24]
	TRMM	TMI	10.65~85.5	9	V, H	1997~2015	Non fixed	1 day	7~63km	35N~35S	[25]
	DMSP	SSM/I	19.35~85.5	7	V, H	1987~2007	06:00; 18:00	1 day	15~69km	Global	[26]
	Nimbus-7	SMMR	6.6~37	10	V, H	1978~1987	12:00; 24:00	6 days	27~148km	Global	[27]
Active microwave	ERS-1/2	SCAT	5.3	1	HH, VV	1991~2011	11:00~14:00	3 days	25km	Global	[28]
	MetOp-A/B	ASCAT	5.255	1	HH, VV	2007~now	09:30; 21:30	1~3 days	25km	Global	[29]
	SMAP	SMAP	1.26	1	VV, HH, VH, HV	2015~now	06:00; 18:00	2~3days	1~3km	Global	[24]

*Ob. Time represents the local time of satellite overpass; MR: Main References; V: Vertical polarization; H: Horizontal polarization; AMSR-E: Advanced Microwave Scanning Radiometer-Earth Observing System; SCAT: Scatterometer; ERS-1/2: European Remote Sensing Satellite-1/2; ASCAT: Advanced Scatterometer; MetOp-A/B: Meteorological operational satellite-A/B; SMAP: Soil Moisture Active Passive; SMMR: Scanning Multichannel Microwave Radiometer; SSM/I: Special Sensor Microwave/Imager; DMSP: Defense Meteorological Satellite Program; TMI; Microwave Imager; TRMM: Tropical Rainfall Measuring Mission; MIRAS: Microwave Imaging Radiometer with Aperture Synthesis; SMOS; Soil Moisture and Ocean Salinity; MWRI: Microwave Radiation Imager; FY3-B: Feng Yun 3-B; FY3-C: Feng Yun 3-C; AMSR-2: Advanced Microwave Scanning Radiometer-2; GCOM-W: Global Change Observation Mission-Water.

(6.9–89 GHz) [12], [13], [23], [24]. The broad frequency range of AMSR-E means that it has the potential to capture vegetation conditions using the higher frequency bands, which are more sensitive to vegetation scattering and canopy water content [12], [13]. This potential, however, would be diminished by the higher radiometric noise and coarse spatial resolution, which render these channels less reliable for parameterizing vegetation transmittance and emission than the fractional vegetation cover (FVC) indicator derived from optical remote sensing. The Advanced Microwave Scanning Radiometer-2 (AMSR-2) sensor, a successor to AMSR-E, provides similar frequency coverage but with improved calibration and data quality [14], [15]. However, the historical AMSR-E data (2002–2011) remain invaluable for long-term SM trend analysis. Compared with the Scanning Multichannel Microwave Radiometer (SMMR) aboard Nimbus-7, AMSR-E has a significantly improved spatial resolution (from 150 to 50 km at 6.925 GHz). It also incorporates all the channels of the previous SMMR, Special Sensor Microwave/Imager (SSM/I) and Tropical Rainfall Measuring Mission' (TRMM) Microwave Image (TMI) sensors (6.925, 10.65, 18.7, 23.8, 36.5, and 89 GHz). The combination of high temporal resolution, a broad frequency range, and global coverage by the AMSR-E sensor enables all-weather, all-time brightness temperature (BT) observations with low sensitivity to atmospheric conditions. This leads to accurate and consistent SM monitoring even under cloudy or rainy conditions, thereby improving our understanding of global hydrological dynamics [16], [17], [18], [19]. Although the AMSR-E sensor stopped operating in 2011 due to an antenna failure, it did acquire nearly ten years of data (2002–2011), which played a crucial role in the global long-term SM data record [10], [11].

Researchers have used AMSR-E observation data to develop various SM retrieval algorithms, such as the semi-empirical algorithms and the SM retrieval algorithm based on the Land Parameter Retrieval Model (LPRM), thus increasing the usefulness for agriculture, climate research, and drought monitoring [30], [31], [32]. At present, AMSR-E data have generated the largest variety of SM products, and there are mainly three types of products.

1) NASA released the official global SM products with a daily resolution of 25-km space grid from 2002 to 2011 [33], [34]. The product used the microwave polarization difference index (MPDI) at the 10.7-GHz band to eliminate the effects of vegetation and surface roughness and used the semi-transcontinental SM inversion algorithm with the minimum monthly MPDI to generate the AMSR-E/NASA SM product [35].
2) JAXA released the AMSR-E/JAXA SM product with a daily resolution of 25 km from 2002 to 2011 by using the radiative transfer equation to simulate different polarization BT data for a different vegetation, soil, and frequency [30].
3) Owe et al. [36] developed the LPRM in 2008, and based on this model, developed AMSR-E/LPRM SM products with a daily spatial resolution of 25 km from 2002 to 2011. Based on radiative transfer theory, LPRM combined SM and emitted radiance to retrieve vegetation density using SM and BT simulations.

The AMSR-E/JAXA lookup table (LUT) approach improves the ability of the product to capture SM under different conditions, but introduces complexity and potential inaccuracies [37]. One key issue is the dependence of the LUT on the accuracy of the input parameters and the underlying assumptions used to model radiative transfer, such as the homogeneity of the land surface, the validity of the τ–ω model approximation, neglecting of multiple scattering effects, and the assumption that atmospheric contributions have been effectively corrected [38], [39], [48]. These assumptions can lead to biases in SM estimates, especially in heterogeneous landscapes where the actual conditions may differ significantly from the modeled scenarios. In addition, the AMSR-E/JAXA has been found to exhibit seasonal biases in certain regions. For example, in the Naqu region of the Tibetan Plateau, it tends to overestimate SM during the summer months (July–August) and underestimate it in winter months (January–February of the next year), likely due to surface freezing and vegetation cover effects [9]. The AMSR-E/LPRM SM product uses a physically based retrieval algorithm that links SM and BT data

through radiative transfer theory. However, its performance over densely vegetated areas is primarily limited by the relatively high observation frequencies (C/X bands), which reduce microwave penetration into soil [41]. In addition, the complexity of accurately modeling the interactions between SM, vegetation, and temperature in the radiation transfer model may also contribute to systematic biases, particularly in regions with dense vegetation or highly variable soil conditions [40], [41]. Furthermore, the reliance of the AMSR-E/LPRM product on ancillary data, such as surface temperature estimates, may introduce additional errors if these inputs are not accurate or representative of the actual conditions [39], [40].

The evaluation and analysis of global long-term microwave SM products and the comparison with other SM products, such as AMSR-E/JAXA and AMSR-E/LPRM, documented the poor sensitivity of the AMSR-E/NASA SM to actual SM [9]. More specifically, the data showed a small interannual and annual variability and could not reflect the interannual, annual, and seasonal variations of SM [9], [34], [42]. These studies showed that the root-mean-square error (RMSE) of AMSR-E/NASA SM products in most of the International Soil Moisture Network (ISMN) observation networks was greater than 0.06 cm^3/cm^3, whereas the unbiased RMSE (ubRMSE) value was substantially smaller (typically below 0.04 cm^3/cm^3) [9]. Since RMSE combines both systematic (bias) and random error components ($RMSE^2 = bias^2 + ubRMSE^2$), this noticeable discrepancy indicates that part of the total retrieval error arises from systematic bias (i.e., a consistent offset between the product and in situ measurements). Such a difference between the RMSE and ubRMSE suggests the existence of a bias component in the AMSR-E/NASA SM product and highlights the need for bias correction. The AMSR-E/NASA SM retrieval algorithm developed by Njoku et al. [32] used the monthly minimum MPDI as a static proxy for vegetation effects, but this approach lacks sensitivity to vegetation dynamics and does not explicitly account for emissivity and transmittance, which may limit its capacity to capture SM variability. Xie et al. [9] explained the large error in the AMSR-E/NASA SM product with the inability of the AMSR-E/NASA SM products to capture annual and seasonal variations in SM. Specifically, their results showed that one of the main reasons might be the inaccurate estimation of the parameters A_0 and A_1 using the minimum monthly MPDI, which account for the effects of vegetation transmittance and emission. In contrast, Chauhan et al. [43] showed that incorporating the Advanced Very High-Resolution Radiometer (AVHRR)-based FVC into a microwave-optical synergy framework significantly improved SM retrieval by explicitly modeling vegetation effects. Thomas et al. [44] demonstrated that incorporating a vegetation indicator into the parameterization of microwave vegetation effects significantly improved the accuracy of SM retrievals over East Asia by better capturing seasonal vegetation dynamics and its influence on surface emissivity and transmittance. These findings indicate the potentiality of dynamic vegetation indicators (e.g., FVC) over the minimum monthly MPDI for improving of AMSR-E SM product.

In this study, the microwave sensor BT data collected by AMSR-E were used. The AMSR-E (NASA, JAXA, and LPRM) SM products (2002–2011) were evaluated. AMSR-E observations of BT were used to retrieve SM using three retrieval methods: 1) the semi-empirical soil water algorithm; 2) the LUT; and 3) the LPRM. The improved algorithm was developed using in situ SM measurements from the ISMN observation networks and the Global Land Surface Satellite FVC (GLASS FVC) dataset. The temporal and spatial statistics of the global AMSR-E/NASA, AMSR-E/JAXA and AMSR-E/LPRM soil water products were compared and analyzed. The semi-empirical algorithm of the AMSR-E/NASA SM product was analyzed, and its parameters were optimized. This algorithm can lead to a low range of SM values that cannot reflect the real interannual and annual soil water changes. By introducing auxiliary data such as vegetation cover, improved SM retrievals were obtained. This article is structured as follows. Section II provides detailed information on the datasets used in this study and the preprocessing applied. Section III introduces the methodology, including the semi-empirical AMSR-E/NASA SM retrieval algorithm, the proposed improvements, and evaluation metrics. Section IV presents the spatiotemporal comparisons of three AMSR-E SM products (NASA, JAXA, and LPRM), the parameter optimization/estimation of the improved AMSR-E/NASA SM retrieval algorithm, the improved SM data product, and its evaluation. Finally, the discussions and main conclusion are presented in Sections V and VI, respectively.

II. Dataset Collection and Preprocessing

A. AMSR-E BT Data

The Aqua satellite was an Earth science satellite launched by NASA on May 4, 2002, carrying six sensors, including the Atmospheric Infrared Sounder (AIRS), the Advanced Microwave Sounding Unit (AMSU), the Clouds and Earth Radiant Energy System (CERES), the Moderate Resolution Imaging Spectroradiometer (MODIS), the Advanced Microwave radiometer AMSR-E, and the Humidity Sensor for Brazil (HSB) [13], [30]. The primary objective of the Aqua satellite mission was to obtain information on the Earth's water cycle, including precipitation, evaporation, atmospheric water vapor, ice, snow cover, and SM. In addition, data on vegetation cover, radiative energy flux, aerosol optical depth (AOD), and temperature were obtained by inversion of observations from the Aqua AMSR-E sensor. The latter was a six-band microwave radiometer (6.92, 10.65, 18.7, 23.8, 36.5, and 89 GHz) [35]. The Sun's synchronous orbit crossed the equator at 1:30 and 13:30 local time. The AMSR-E sensor had both horizontal and vertical dual polarization modes and was widely used for global-scale SM retrievals. Global-scale Level 1 (L1) BT data (2002~2011) observed by the AMSR-E sensor were generated by JAXA and then were used to develop and produce Level 2 (L2) and 3 (L3) application products (https://nsidc.org/data/AE_Land3/versions/2).

B. Three Global-Scale AMSR-E SM Products

To analyze the spatiotemporal characteristics of the AMSR-E/NASA SM product, three AMSR-E SM products

TABLE II
MAIN INPUTS OF THE RETRIEVAL ALGORITHMS OF THE AMSR-E/NASA, JAXA, AND LPRM SM PRODUCTS

	NASA [32]	**JAXA** [48]	**LPRM** [31]
Forward theoretical model	The simplified RTM, i.e., $\tau - w$ model	the fully physically RTM	The simplified RTM i.e., $\tau - w$ model
SM retrieval algorithm	The semi-empirical algorithm	The LUT algorithm	LPRM
Bands of BT	10.65 GHz and 18.7 GHz	6.925 GHz, 10.65 GHz and 18.7 GHz	10.65 GHz and 37 GHz
Land surface roughness	Not considered	The simulation using AIEM [49]	Not considered
Vegetation parameter	The linear model: $g^*=\beta_0+\beta_1 * \ln(MPDI^*_{10.7})$ (g^* is the vegetation parameter related to g^* is the baseline parameter, interpreted as equivalent vegetation water content; $MPDI^*_{10.7}$ is the minimum monthly MPDI at 10.7GHz)	Negligible (VWC≤0.1 kg/m^2)	The internal analytical approach for Vegetation optical depth ($\tau_{c(H)}$): $\tau_{c(H)} = C_1 * \ln(MPDI)^3 + C_2 * \ln(MPDI)^2 + * \ln(MPDI) + C_4$.
Soil temperature (Ts) and vegetation canopy temperature (Tv)	Not considered	A LUT composed by the soil physical temperature, SM, BT (10.65 GHz) vertical polarization and an index named dBT calculated as following: $dBT=BT_{(18.7GHz, H)}-BT_{(10.65GHz, V)}$	Assuming that Ts and Tv are approximately equivalent temperatures (T_{eff}): $T_{eff}=0.688*BT_{(37GHz, V)}+101.126$.
Vegetation single scattering albedo (w)	w≈0	DMRT [50]	/
Dielectric constant of soil	Dobson model [51]	Dobson model [51]	Wang and Schmugge model [52]
Atmosphere effect	Negligible	Negligible	Negligible

*RTM: Radiative Transfer Model; LUT: Look-Up-Table; LPRM: Land Parameter Retrieval Model; BT: Brightness Temperature; VWC: Vegetation Water Content; MPDI: Microwave Polarization Difference Index; H: Horizontal polarization; V: Vertical polarization; AIEM: Advanced Integration Equation Model; DMRT: Dense Media Radiative Transfer Theory.

(i.e., AMSR-E/NASA, AMSR-E/JAXA, and AMSR-E/LPRM) were selected and compared with each other. These three AMSR-E SM products used the same BT observations by the AMSR-E sensor, but used a different SM retrieval algorithm (see Table II), i.e., the semi-empirical SM algorithm using the MPDI (AMSR-E/NASA), the LUT (AMSR-E/JAXA), and the LPRM (AMSR-E/LPRM), respectively [13], [30], [31], [32]. The AMSR-E/NASA and AMSR-E/LPRM SM products have been published by the National Snow and Ice Data Center Distributed Active Archive Center (NSIDC DAAC) (https://nsidc.org/data/amsre/data\summaries/index.html), and the AMSR-E/JAXA SM product has been released by JAXA (https://gcom-w1.jaxa.jp/auth.html). The temporal resolution of AMSR-E (NASA, JAXA, and LPRM) SM products was one day, the spatial grid resolution was 25 km, and the unit of SM was the soil volumetric water content (cm^3/cm^3).

C. Global FVC Dataset

Jia et al. [45], [46] and Yang et al. [47] developed the GLASS FVC dataset. The dataset can be downloaded for free from the National Earth System Science Data Center, National Science and Technology Infrastructure of China (http://www.geodata.cn). The product was based on machine learning methods by training a model of the relationship between surface reflectivity and vegetation cover. Thus, the vegetation cover was obtained by inversion of the observations by AVHRR on board the NOAA series of weather satellites [47]. The temporal coverage is from 1982 to 2015, the temporal resolution is eight days, and the spatial resolution is 5 km. To be consistent with the spatial resolution of AMSR-E/NASA SM products, the GLASS FVC data were resampled to a spatial resolution of 25 km by averaging the 5 × 5 pixels.

D. In Situ Measurements

In this study, the 19 in situ observation networks (804 sites, Fig. 1) from ISMN were divided into two geographically nonoverlapping subsets for different purposes: one subset (192 sites) for parameter optimization of the improved AMSR-E/NASA retrieval algorithm, and another (612 sites) for independent evaluation (see Table III). This division avoids spatial dependence between calibration and evaluation datasets.

The ISMN stands as a collaborative effort initiated by key entities, including the Global Energy and Water Cycle Experiment (GEWEX), Committee on Earth Observation Satellites (CEOS), Global Climate Observing System—Terrestrial Observation Panel for Climate (GCOS-TOPC), Group on Earth Observations (GEO), and Global Terrestrial Network-Hydrology (GTN-H) [53], [54]. This repository has been established and operated with the financial support of European Space Agency's Earth Observation Program and the generous contributions of scientists worldwide. The SM data curated on the ISMN platform serves as an indispensable resource for the evaluation and refinement of global satellite SM products, as well as for the development of land surface, climate, and hydrological models [54], [55]. In this study, global measurements of SM from the ISMN networks were downloaded from the year 2000 onward. These datasets covered five continents, including Africa (AMMA-CATCH and DAHRA), Asia (CTP_SMTMN, MAQU, SKKU, and MySMNet), Europe (HOBE, FMI, SMOSMANIA, TERENO, HYDROL-NET_PERUGIA, RSMN, REMEDHUS, and VAS), North America (SNOTEL, USCRN, and USDA-ARS), and Oceania (OZNET and SASMAS), which were utilized for the evaluation and analysis of global long-term microwave SM products. Fig. 1 shows the spatial distribution of 19 in situ observation networks (804 sites) from ISMN on European Space Agency-Climate Change Initiative (ESA-CCI)-Land Cover (LC)-map, 2015.

Of the 19 in situ observation networks, six networks (i.e., CTP_SMTMN in China, AMMA-CATCH in Africa, REMEDHUS and VAS in Spain, HOBE in Denmark, and

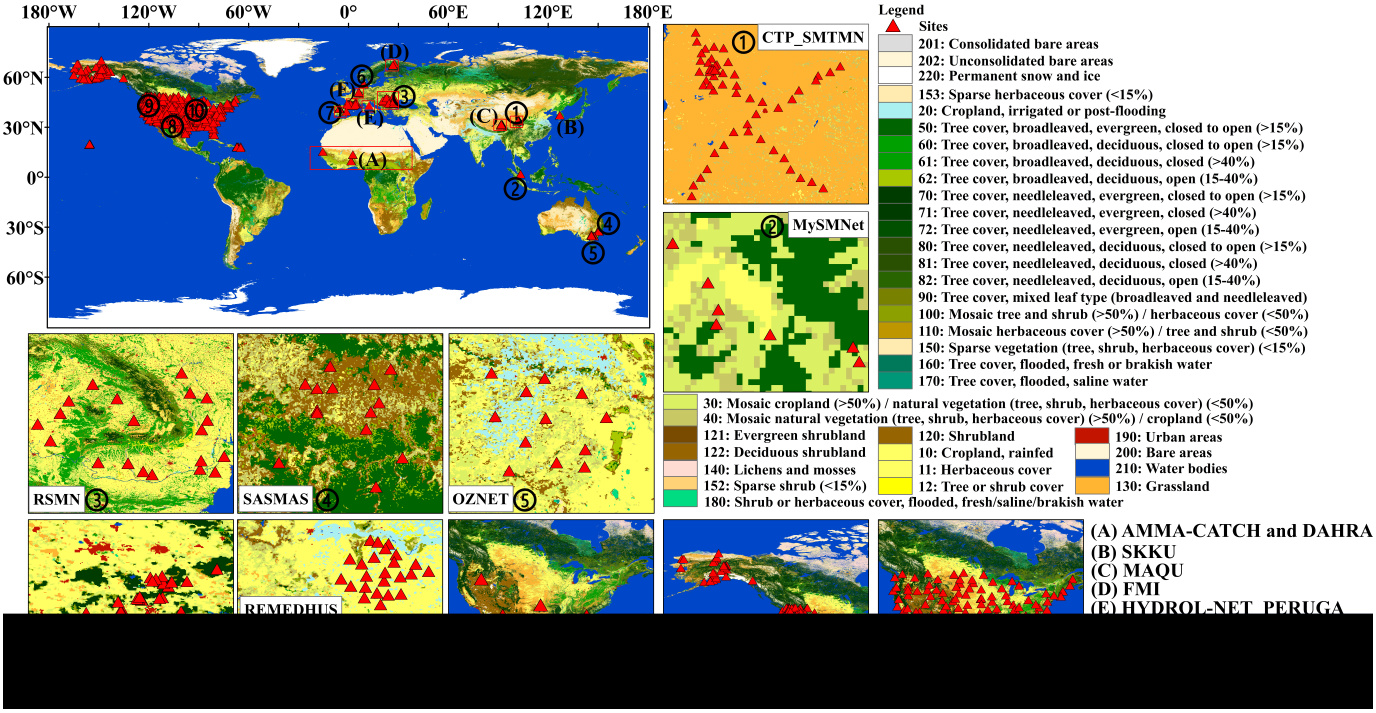

Fig. 1. In situ observation networks from the ISMN that were used in this study; land cover (from ESA-CCI Land Cover map, 2015) was also shown.

TABLE III

INFORMATION OF IN SITU SM MEASUREMENTS FROM 804 SITES OF 19 NETWORKS OF THE ISMN PROGRAM USED FOR THE MODEL PARAMETER OPTIMIZATION (192 SITES OF SUBSET 1) AND FOR RESULTS VALIDATION (612 SITES OF SUBSET 2) IN THIS STUDY (ST: SOIL TEMPERATURE; AT: AIR TEMPERATURE; P: PRECIPITATION; SD: SOIL DEPTH; N: NUMBER OF SITES OF IN SITU MEASUREMENTS IN EACH NETWORK)

Use for	Ob. Networks	Countries	*N*	SD	Parameters	Periods
Subset 1: Spatiotemporal analysis and parameter optimization	CTP_SMTMN	China	57	5 cm	SM, ST	2010.08.01~2016.09.19
	AMMA-CATCH	Benin, Niger, Mali	7	5 cm	SM	2006.01.01~2014.12.31
	CARBOAFRICA	Sudan	1	5 cm	SM, ST, AT, P	2005.02.01~2010.01.20
	DAHRA	Senegal	1	5 cm	SM, ST, AT, P	2002.07.04~2016.01.01
	REMEDHUS	Spain	24	5 cm	SM, ST	2007.05.17~2017.12.31
	VAS		2	5 cm	SM, ST, AT	2010.01.01~2012.01.01
	HOBE	Denmark	32	5 cm	SM, ST	2009.09.08~2019.03.13
	SMOSMANIA	France	21	5 cm	SM, ST	2007.01.01~2019.01.01
	FMI	Finland	1	5 cm	SM, ST, AT	2007.01.25~2020.09.05
	TERENO	Germany	1	5 cm	SM, ST, AT, P	2009.12.31~2020.08.10
	USDA-ARS	USA	4	5 cm	SM, ST	2002.06.01~2009.07.31
	SNet_ARM_USA		29	5 cm	SM, ST	2001.01.01~2015.03.26
	DNet_BNZ-LTER_USA		12	5 cm	SM, TA	2001.01.01~2013.01.01
Subset 2: Evaluation	OZNET	Australia	20	5 cm	SM, ST	2001.09.12~2018.08.27
	SASMAS		14	5 cm	SM, ST	2005.12.31~2007.12.31
	MAQU	China	20	5 cm	SM, ST	2008.06.30~2010.07.31
	HYDROL-NET_PERUGIA	Italy	2	5 cm	SM, ST	2010.01.01~2013.12.31
	SNOTEL	USA	441	5 cm	SM, ST	1980.10.01~2020.10.27
	USCRN		115	5 cm	SM, ST	2000.11.15~2020.10.26

DNet_BNZ-LTER_USA in United States) are relatively dense, with more sites available within the AMSR-E/NASA SM product pixels. These networks are multiscale observation networks with 10, 25, 50, and 100 km. The other observation networks are sparse, with only one observation station within an AMSR-E/NASA SM product pixel. If there are more than two sites within the same pixel of AMSR-E/NASA SM product, the average in situ measured SM at all sites in the same pixel was used as the "true value" for this study. According to the ESA-CCI-LC map (2015), the land cover types of 804 sites were mainly grassland, cropland, and forest, accounting for 37%, 33%, and 10% of the total area, respectively.

Subset 1 was used to analyze three AMSR-E SM products (i.e., NASA, JAXA, and LPRM) and to optimize the parameters of the improved AMSR-E/NASA SM retrieval algorithm proposed in this study. This subset included 13 in situ observation networks (CTP_SMTMN, AMMA-CATCH, CARBOAFRICA, DAHRA, REMEDHUS, VAS, HOBE, SMOSMANIA, FMI, TERENO, SNet_ARM_USA, USDA-ARS, and DNet_BNZ-LTER_USA), which had relatively uniform land cover and a dense site distribution. These 13 networks were located in Asia, Europe, Africa, and North America, and comprised a total of 192 sites.

Subset 2 consisted of six networks (OZNET, SASMAS, MAQU, HYDROL-NET_PERUGIA, SNOTEL, and USCRN), totaling 612 sites in Australia, Asia, Europe, and North America, and was used exclusively for the independent evaluation of the AMSR-E SM products (NASA, JAXA,

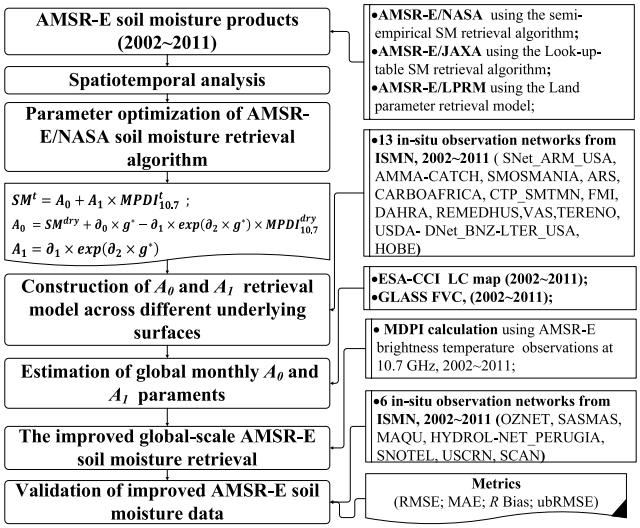

Fig. 2. Flowchart of the improvements of the AMSR-E/NASA SM retrieval algorithm and data product.

and our improved retrieval). The second subset included six observation networks (i.e., OZNET, SASMAS, MAQU, HYDROL-NET_PERUGIA, SNOTEL, and USCRN) for evaluating the AMSR-E (NASA, JAXA, and our SM products), with two networks in Australia, one in Asia, one in Europe, and three in North America in United States. These six networks in subset 2 comprised a total of 612 sites.

III. Methodology

A. Approach Overview

This study proposed an approach to produce global daily-scale AMSR-E SM product data (2002–2011) with improved accuracy compared with AMSR-E/NASA SM data, capable of reflecting the characteristics of intra-annual and interannual variability of SM (see Fig. 2). First, the spatial and temporal distribution of the AMSR-E/NASA, AMSR-E/JAXA and AMSR-E/LPRM SM products were compared, as well as the spatial distributions of the monthly minimum MPDI at 10.7-GHz data, vegetation cover data, and AMSR-E/NASA SM data product. Then, for the global land area, based on the simplified AMSR-E/NASA SM retrieval algorithm [see (5)], the AMSR-E SM algorithm was optimized using in situ SM measurements and vegetation cover data and the improved data products were generated following the procedures: 1) A_1 and A_0 parameters were obtained for different land cover types by fitting the in situ SM measurements from the 13 ISMN observation networks; 2) the relationship between the A_1 and A_0 parameters and monthly vegetation cover was analyzed and optimized; and 3) using the new global A_1 and A_0 parameter sets, the global daily AMSR-E MPDI data were used to generate an improved global SM dataset.

B. Semi-Empirical AMSR-E/NASA SM Retrieval Algorithm

The original AMSR-E/NASA SM retrieval algorithm was a multifrequency, multipolarization method. In this algorithm, the coefficients were determined by minimizing the difference between the BT simulated with the simplified radiative transfer equation and the AMSR-E BT observations [9], [32]. Njoku et al. [32] developed a linear method to retrieve SM from AMSR-E satellite observations, using the MPDI value and empirical coefficients to retrieve SM. The formulas are as follows:

$$\mathrm{SM}^t - \mathrm{SM}^{\mathrm{dry}} = a_0 \cdot g^* + a_1 \cdot \left(\mathrm{MPDI}^t_{10.7} - \mathrm{MPDI}^{\mathrm{dry}}_{10.7}\right) \cdot \exp\left(a_2 \cdot g^*\right) \quad (1)$$

$$\mathrm{MPDI}_{10.7} = \left(T_{B(10.7V)} - T_{B(10.7H)}\right) / \left(T_{B(10.7V)} + T_{B(10.7H)}\right) \quad (2)$$

$$g^* = \beta_0 + \beta_1 \cdot \ln\left(\mathrm{MPDI}^*_{10.7}\right) \quad (3)$$

where t is the day of the year (DoY), SM^t is the SM at time t, $\mathrm{SM}^{\mathrm{dry}}$ is the minimum SM value (default is 0.05 $\mathrm{cm}^3/\mathrm{cm}^3$), $\mathrm{MPDI}^t_{10.7}$ is the MPDI at 10.7 GHz value on day t, $\mathrm{MPDI}^{\mathrm{dry}}_{10.7}$ is the annual minimum MPDI value at 10.7 GHz under dry soil conditions, $T_{B(10.7V)}$ is the BT for vertical polarization at 10.7 GHz, $T_{B(10.7H)}$ is 10.7-GHz BT for horizontal polarization, and g^* is the baseline parameter, accounting for the influence of vegetation and surface roughness. g^* was estimated by $\mathrm{MPDI}^*_{10.7}$ (i.e., the minimum MPDI at a monthly scale), which can be interpreted as the equivalent vegetation water content ($\mathrm{kg/m}^2$) [37]. The a_0, a_1, a_2,β_0, and β_1 are empirical coefficients. In order to retrieve SM, the a_0, a_1, a_2,β_0, and β_1 parameter values need to be obtained. Jackson et al. [37] determined the a_0, a_1, a_2,β_0, and β_1 parameters by taking AMSR-E observations from Chad, Sudan, and the Central African Republic, where surface SM was low, and assuming an average SM of 0.1 $\mathrm{cm}^3/\mathrm{cm}^3$, thus allowing the a_0, a_1, a_2,β_0, and β_1 parameters to be determined [37].

C. Improving the AMSR-E/NASA SM Retrieval Algorithm

1) Estimation of Model Parameters: In this study, we rewrote the semi-empirical AMSR-E/NASA SM retrieval algorithm [see (1)] as follows:

$$\mathrm{SM}^t = \mathrm{SM}^{\mathrm{dry}} + a_0 \cdot g^* - a_1 \exp\left(a_2 \cdot g^*\right) \cdot \mathrm{MPDI}^{\mathrm{dry}}_{10.7} + a_1 \cdot \exp\left(a_2 \cdot g^*\right) \times \mathrm{MPDI}^t_{10.7}. \quad (4)$$

Therefore, the semi-empirical AMSR-E/NASA SM retrieval algorithm can be rewritten as a relationship between the SM and MPDI at 10.7 GHz and A_1 and A_0 parameters, as follows:

$$\mathrm{SM}^t = A_0 + A_1 \cdot \mathrm{MPDI}^t_{10.7}, \quad (t = 1, 2, \ldots, 365) \quad (5)$$

$$A_0 = \mathrm{SM}^{\mathrm{dry}} + a_0 \cdot g^* - a_1 \exp\left(a_2 \cdot g^*\right) \cdot \mathrm{MPDI}^{\mathrm{dry}}_{10.7} \quad (6)$$

$$A_1 = a_1 \cdot \exp\left(a_2 \cdot g^*\right) \quad (7)$$

where A_1 parameter determines the range of SM^t values, while A_0 parameter determines the magnitude of the initial value of SM^t. Both A_1 and A_0 parameters are related to g^*, reflecting the vegetation emittance and transmittance. If a good global A_0 and A_1 parameter set could be obtained, the MPDI data could be used to further improve the global AMSR-E/NASA SM data product [9]. The semi-empirical AMSR-E/NASA SM retrieval algorithm considers only the impact of vegetation, ignoring the impact of surface roughness, and uses the monthly minimum MPDI at 10.7 GHz, i.e., $\mathrm{MPDI}^*_{10.7}$ to represent the

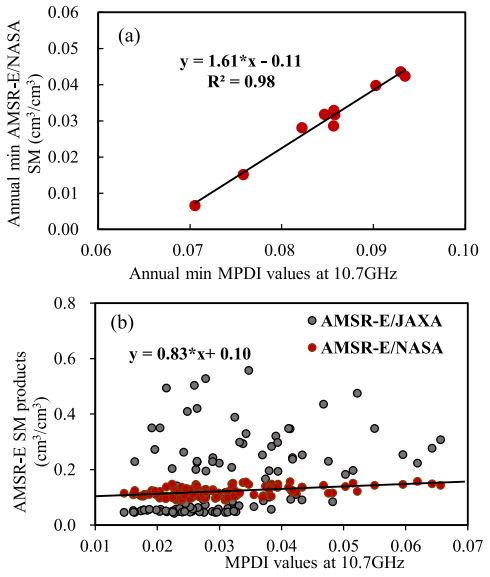

Fig. 3. (a) Variations in annual minimum MPDI values at 10.7 GHz under dry soil conditions (i.e., the annual minimum AMSR-E/NASA SM values are less than 0.05 cm^3/cm^3) from 2002 to 2011 in north of Sudan. (b) Scatter plots between the monthly average AMSR-E/NASA (or JAXA) SM and MPDI values at 10.7 GHz in the Naqu, Tibetan Plateau.

impact of vegetation [see (3)]. By substituting (3) into (6) and (7), respectively, the relationships of A_0 and A_1 parameters with the monthly minimum MPDI at 10.7 GHz are obtained, and the equations to calculate A_0 and A_1 parameters are

$$A_0 = c_0 + c_1 \cdot \ln\left(\mathrm{MPDI}^*_{10.7}\right) - abc_2 \cdot \mathrm{MPDI}^*_{10.7} \tag{8}$$

$$A_1 = a \cdot \left(\mathrm{MPDI}^*_{10.7}\right)^b \tag{9}$$

$$a = a_1 \exp\left(a_2\beta_0\right), \quad b = a_2\beta_1, \quad c_1 = a_0\beta_1 \tag{10}$$

$$c_0 = \mathrm{SM}^{\mathrm{dry}} + a_0\beta_0, \quad c_2 = \mathrm{MPDI}^{\mathrm{dry}}_{10.7} \tag{11}$$

where a, b, c_0, c_1 and c_2 are the coefficients. a, b, and c_1 are only related to the constant coefficients a_0, a_1, a_2, β_0, and β_1. c_0 coefficient is related to $\mathrm{SM}^{\mathrm{dry}}$ (i.e., the minimum SM value, and the default value is generally 0.05 cm^3/cm^3). The c_2 coefficient is equal to the $\mathrm{MPDI}^{\mathrm{dry}}_{10.7}$, i.e., the annual minimum MPDI value under dry soil conditions.

In (8) and (9), the parameters A_0 and A_1 can be represented as a linear or exponential (when $b \neq 1$) relationship with the monthly minimum MPDI at 10.7 GHz (i.e., $\mathrm{MPDI}^*_{10.7}$). For the AMSR-E/NASA SM inversion algorithm, the parameters A_1 and A_0 are related to the monthly minimum MPDI at 10.7 GHz. g^* is calculated using the monthly minimum MPDI at 10.7 GHz to characterize the influence of vegetation. Since this affects A_0 and A_1 parameters, the retrieved SM is ultimately affected. Theoretically, the AMSR-E/NASA SM data products could be improved if the values of the A_0 and A_1 parameters were accurate. The variations of $\mathrm{MPDI}^{\mathrm{dry}}_{10.7}$ and annual minimum SM pixel values of the AMSR-E/NASA SM product from 2002 to 2011 in the north of Sudan and the scatter plots between the monthly average AMSR-E/NASA (or JAXA) SM values and MPDI at 10.7 GHz in the CTP_SMTMN network were shown in Fig. 3(a) and (b).

The relationship between the annual minimum SM pixel values of the AMSR-E/NASA SM product and the $\mathrm{MPDI}^{\mathrm{dry}}_{10.7}$ values in the north of Sudan are linear and have high correlation, i.e., 0.98, as shown in Fig. 3(a). This indicates that in the arid desert areas (no vegetation), such as the north of Sudan, the annual AMSR-E/NASA SM is approximately linearly correlated with MPDI values, i.e., A_0 and A_1 parameters in (5) can be considered as constant. In addition, in the Naqu area, Tibetan Plateau, there is also a linear relationship ($y = 0.83^*x + 0.10$) between the monthly average AMSR-E/NASA SM and MPDI values at 10.7 GHz [9], but the variation of AMSR-E/NASA SM values with MPDI at 10.7 GHz is very low in Fig. 3(b). Conversely, there is a nonlinear relationship between the AMSR-E/JAXA SM and MPDI at 10.7 GHz.

2) Global Mapping of A_0 and A_1: Theoretically, A_0 and A_1 parameters are affected by vegetation, thus A_0 and A_1 parameters vary with the amount of vegetation. Therefore, it is necessary to develop a method to estimate A_0 and A_1 parameters of the AMSR-E/NASA SM retrieval algorithm as a function of vegetation biomass/fractional cover. In this study, the SM retrieval algorithm based on (5) was improved

$$\mathrm{SM}^t = A_0 + A_1 \cdot \mathrm{MPDI}^t_{10.7}, \quad t = 1, 2, \ldots, 365 \tag{12}$$

$$A_1 = f\left(\mathrm{MPDI}^*_{10.7}\right) \text{ or } A_1 = f(\mathrm{FVC}) \tag{13}$$

$$A_0 = f\left(\mathrm{MPDI}^*_{10.7}\right) \text{ or } A_0 = f(\mathrm{FVC}) \tag{14}$$

where t is the DoY, SM^t is the SM with time, $\mathrm{MPDI}^t_{10.7}$ is the MPDI value at 10.7 GHz on day t, $\mathrm{MPDI}^*_{10.7}$ is the monthly minimum MPDI values at 10.7 GHz, and A_0 and A_1 can be interpreted as emittance and transmittance [see (13) and (14)]. Equation (12) shows the relationship between observed microwave signals and SM by separating vegetation transmittance (A_1), emittance (A_0), and soil emittance. By modeling the parameters of A_0 and A_1 as functions of FVC, we aim to improve the estimation of below-canopy soil surface emittance, thereby enhancing the accuracy of AMSR-E SM retrieval.

3) Improved Global-Scale AMSR-E SM Retrieval: In this study, A_0 and A_1 parameter values were estimated by fitting (12) to the daily in situ SM measurements and MPDI at 10.7 GHz. The estimated A_1 and A_0 values were classified into five main land cover categories according to the land cover type (ESA-CCI Land Cover map) at each site where in situ SM measurements were available, i.e., cropland, grassland, forest, bare soil, and others. The cropland category includes the rainfed and irrigated croplands. The grassland category includes both natural temperate grasslands and savanna-type ecosystems. Forest category includes various types (e.g., broadleaf, needleleaf, herbaceous, and mixed forests). The bare soil category includes the consolidated and unconsolidated bare areas. The others category aggregates shrubland (evergreen and deciduous) and all of the mosaic land types (e.g., forest, shrubland, and cropland). Finally, A_1 and A_0 values were correlated with $\mathrm{MPDI}^t_{10.7}$ and FVC to obtain a global estimator.

D. Evaluation Metrics

In this study, five metrics, i.e., mean absolute error (MAE, cm^3/cm^3), RMSE (cm^3/cm^3), ubRMSE (cm^3/cm^3), Bias (cm^3/cm^3), and correlation coefficient (R), were employed

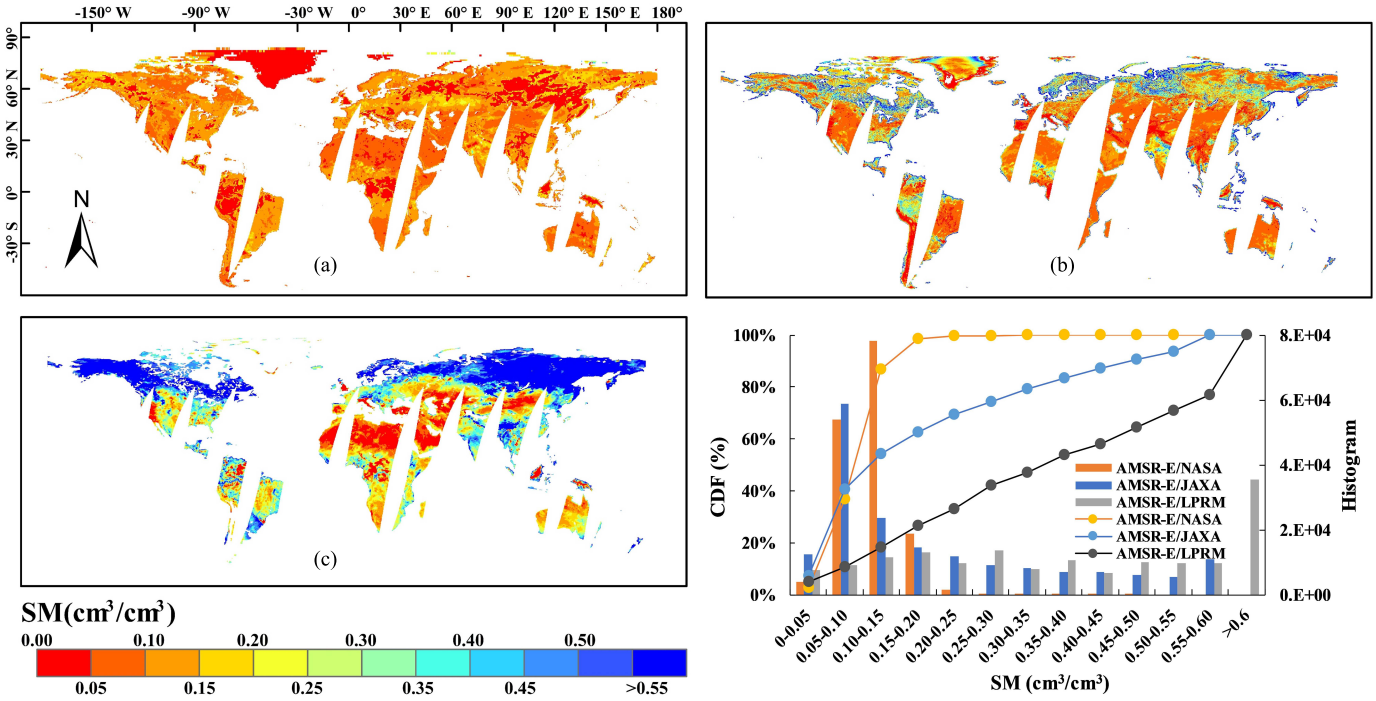

Fig. 4. Spatial distribution patterns and cdf statistics of (a) AMSR-E/NASA, (b) AMSRE/JAXA, and (c) AMSR-E/LPRM SM (cm^3/cm^3) product data on August 1, 2010.

to evaluate the improved AMSR-E SM product against in situ SM measurements (see Table III). The formulas of the five evaluation metrics are

$$\mathrm{MAE} = \sum_{i=1}^{N} \left(\mathrm{SM}_i^E - \mathrm{SM}_i^O\right)/N \tag{15}$$

$$\mathrm{RMSE} = \sqrt{\sum_{i=1}^{N} \left(\mathrm{SM}_i^E - \mathrm{SM}_i^O\right)^2/N} \tag{16}$$

$$\mathrm{ubRMSE} = \sqrt{\sum_{i=1}^{N} \left(\left(\mathrm{SM}_i^E - \overline{\mathrm{SM}^E}\right) - \left(\mathrm{SM}_i^o - \overline{\mathrm{SM}^o}\right)\right)^2/N} \tag{17}$$

$$\mathrm{Bias} = \left|\overline{\mathrm{SM}^E} - \overline{\mathrm{SM}^o}\right| \tag{18}$$

$$R = \frac{\mathrm{cov}\left(\mathrm{SM}_i^E, \mathrm{SM}_i^O\right)}{\sigma_{\mathrm{SM}_i^E}\sigma_{\mathrm{SM}_i^O}}, \quad \begin{cases}\mathrm{cov}\text{: covariance} \\ \sigma\text{ : standard deviation}\end{cases} \tag{19}$$

where SM_i^E (cm^3/cm^3) is the estimated SM value on the ith day, $\overline{\mathrm{SM}^E}$ (cm^3/cm^3) is the mean value of the estimated SM value, SM_i^O (cm^3/cm^3) is the in situ measured SM on the ith day, $\overline{\mathrm{SM}^o}$ is the mean value of in situ measured SM, and N is the number of measurements.

IV. Results

A. Spatiotemporal Analysis of AMSR-E/NASA SM Product

1) Comparison of AMSR-E/JAXA and LPRM SM Products in Space and Time: The spatial distribution of the AMSR-E/NASA SM product was compared with the AMSR-E/JAXA and AMSR-E/LPRM SM products. Specifically, we used global distribution maps, histograms, and cumulative distribution function (cdf) curves of the AMSR-E/NASA, AMSR-E/JAXA, and AMSR-E/LPRM SM products with a spatial grid resolution of 25 km on August 1, 2010 (see Fig. 4). These maps, histograms, and cdf curves highlighted the spatial differences in SM estimates in different regions, reflecting the specific characteristics of each AMSR-E (NASA, JAXA, and LPRM) product and data processing methodologies.

The histogram of the AMSR-E/NASA SM data shows that the SM estimates are mainly concentrated in the 0.05–0.15-cm^3/cm^3 range. The cdf curve shows that the cumulative percentage of SM values increases rapidly in the lower moisture range, reaching 100% before 0.15 cm^3/cm^3. This indicates that a large proportion of the SM values in the AMSR-E/NASA SM product are in the lower range. The histogram of the AMSR-E/JAXA data shows a prominent peak in the 0.10–0.15-cm^3/cm^3 range, indicating the highest frequency of SM values within this narrow range. The cdf curve shows a rapid increase in cumulative percentage, becoming steady after 0.15 cm^3/cm^3. This indicates that the AMSR-E/JAXA data are also concentrated in a narrow SM range, with SM values slightly higher than the AMSR-E/NASA SM, but still at the lower end. The histogram and cdf curve of the AMSR-E/LPRM data show a wider range of SM values, from 0.0 to 0.6 cm^3/cm^3. The cdf curve shows a gradual increase in the cumulative percentage over the whole range, approaching 100% only around 0.60 cm^3/cm^3. This implies that the AMSR-E/LPRM data are evenly distributed, making it suitable for monitoring SM in a wide range of conditions, from arid to humid environments.

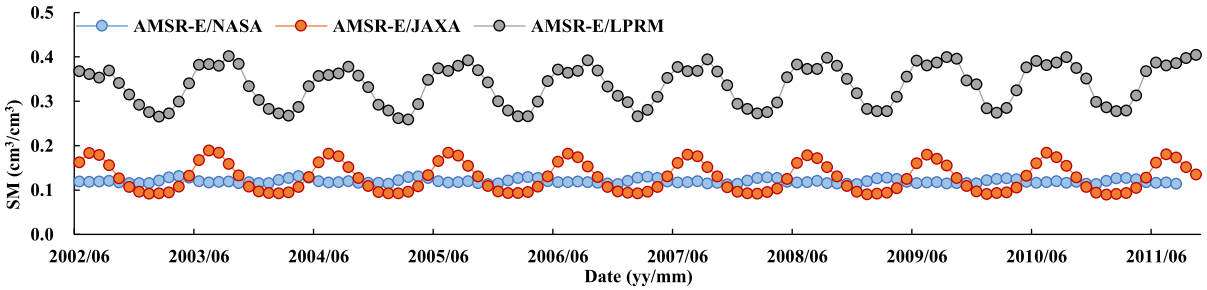

Fig. 5. Monthly temporal evolutions of global average SM (cm^3/cm^3) values of AMSR-E (NASA, JAXA, and LPRM) SM products from 2002 to 2011.

By comparing the global AMSR-E/JAXA and AMSR-E/LPRM SM products with the AMSR-E/NASA SM products on August 1, 2010 (see Fig. 4), the global AMSR-E/NASA SM product value is from 0 to 0.3 cm^3/cm^3, and the change is small, which can hardly capture the spatial variability of SM. This problem has affected the application of AMSR-E/NASA SM products in agricultural drought monitoring, global climate research, and other fields [34], [42].

The AMSR-E/NASA map shows SM predominantly in the lower range, as indicated by the extensive areas covered in red and orange, especially over arid and semi-arid regions such as the Sahara Desert, central Australia, and the Middle East. This is consistent with the histogram/cdf analysis, which suggests a concentration of SM values in the 0.05–0.15-cm^3/cm^3 range. The sparsely distributed green and blue areas indicate regions with higher SM content, but these are limited, emphasizing the tendency of the product to underestimate actual SM. The AMSR-E/JAXA map shows a wider distribution of SM, with notable blue and green patches spread across temperate and humid regions, such as North America, Europe, and parts of Asia. This variation suggests that AMSR-E/JAXA captures a wider range of SM conditions than the AMSR-E/NASA. The map still shows substantial red and orange areas, consistent with the product histogram peak in the 0.10–0.15-cm^3/cm^3 range. The AMSR-E/LPRM map shows the widest range of SM values, with significant coverage in the blue and green areas, particularly at higher latitudes and in regions of high rainfall. This product shows more extensive regions of higher SM (0.00–0.60 cm^3/cm^3), consistent with the histogram/cdf, which indicates a more even distribution of SM values.

Overall, the global distribution maps, histograms, and CDFs of the AMSR-E/NASA, AMSR-E/JAXA, and AMSR-E/LPRM products highlight the distinct characteristics and capabilities of these three products. Both AMSR-E/NASA, and AMSR-E/JAXA underestimate SM, while AMSR-E/LPRM is applicable over a wider range of moisture conditions.

The temporal evolutions of the global monthly average SM from 2002 to 2011 according to the AMSR-E NASA, JAXA, and LPRM data products at a spatial resolution of 25 km were compared (see Fig. 5).

The intra-annual and interannual variability of SM is evident in the AMSR-E/JAXA and AMSR-E/LPRM SM products. In January and February of each year, the SM reaches the annual minimum, while in August and September, the SM value is the highest. In addition, the annual range of SM is quite different for AMSR-E/LRPM and AMSR-E/JAXA SM, i.e., 0.1–0.20 (AMSR-E/JAXA) versus 0.27–0.41 cm^3/cm^3(AMSR-E/LRPM). Compared with the AMSR-E/JAXA and AMSR-E/LPRM SM products, the AMSR-E/NASA SM product hardly changes with time, i.e., the AMSR-E/NASA SM product value is not sensitive to the intra-annual and interannual variability of SM. From 2002 to 2011, the global monthly average SM value of the AMSR-E/NASA SM product is close to a constant value, i.e., 0.12 cm^3/cm^3.

2) Comparison of SM With FVC and Minimum MPDI at 10.7 GHz: According to the AMSR-E/NASA SM retrieval algorithm, the monthly minimum MPDI value at 10.7 GHz is used as a parameter to characterize the impact of vegetation. Therefore, it is necessary to compare the global spatial distribution of monthly minimum MPDI at 10.7 GHz, vegetation cover, and AMSR-E/NASA SM. This was done for four months in 2010, namely, January (winter), April (spring), July (summer), and October (autumn) (see Fig. 6).

The spatial distribution of the AMSR-E/NASA SM products in January, April, July, and October 2010 is not significantly different and does not change with time, with no apparent seasonality. The same is true for the monthly minimum MPDI data at 10.7 GHz. Most of the global vegetation cover in northern Asia in July 2010 (> 0.6) was significantly higher than that in January, April, and October 2010 (range 0.3–0.5). In this region, most of the AMSR-E/NASA SM values in January, April, and July–October 2010 are in the range of 0.20–0.25, with no significant change. Similarly, most of the monthly minimum MPDI values at 10.7 GHz in this region from January, April, and July to October 2010 are in the range of 0–0.02, with little variation.

The global monthly MPDI data at 10.7 GHz change little over time, and it is difficult to detect changes in vegetation cover over time. Therefore, the monthly minimum MPDI at 10.7 GHz was replaced by the FVC as an indicator of vegetation cover in this study. A relationship between A_0 and A_1 and FVC was established to estimate these parameters. Finally, the global A_0 and A_1 parameter sets and the MPDI data calculated from the AMSR-E BT were used to retrieve the global AMSR-E SM data.

B. Estimation of Global Monthly A_0 and A_1 Parameters

1) Method for Estimating A_0 and A_1 Parameters: The SM measurements were collected within 13 observation networks (see Table III). A relationship linking SM to A_0 and A_1, monthly minimum MPDI at 10.7-GHz scale, and FVC was

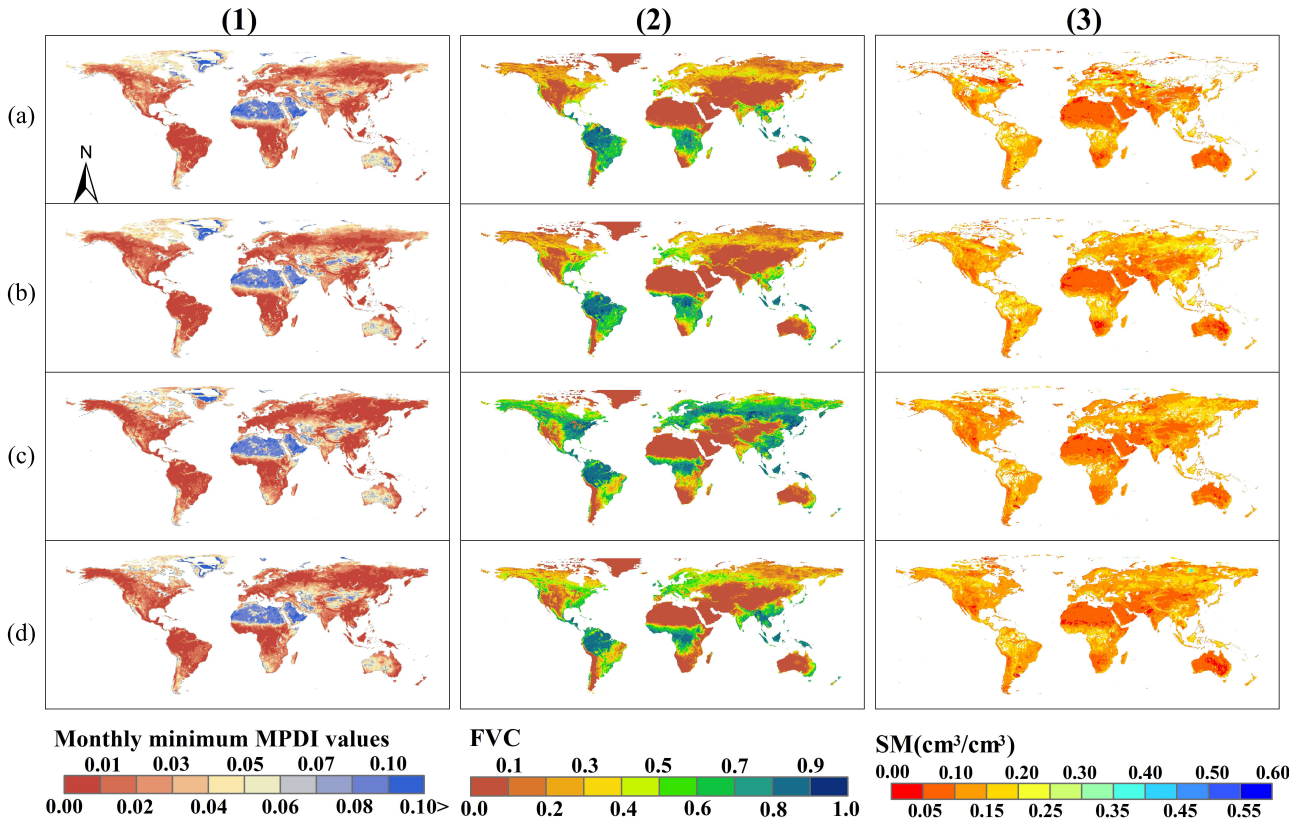

Fig. 6. Monthly minimum MPDI at (1) 10.7 GHz, (2) FVC, and (3) AMSR-E/NASA SM (cm^3/cm^3) in (a) January, (b) April, (c) July, and (d) October, 2010.

fit to the SM measurements collected within 13 observation networks. These sites were mainly located in areas of cropland, grassland, forest, and bare soil. Therefore, a relationship was obtained for each land cover type, i.e., cropland, grassland, forest, and bare soil (see Fig. 7).

In general, A_1 increases with the monthly minimum MPDI at 10.7 GHz, while A_0 decreases. Furthermore, the response to MPDI in vegetated areas is weakly sensitive to A_1. The scatter plots of A_1 and A_0 versus FVC show that A_1 first decreases and then increases with FVC, while A_0 first increases and then decreases. In addition, A_0 is more significantly correlated with FVC than the monthly minimum MPDI at 10.7 GHz.

Two relationships were established to estimate A_1 and A_0 for bare soil, grassland, cropland, and forest area using retrievals of FVC and monthly minimum MPDI at 10.7 GHz: 1) FVC only and 2) monthly minimum MPDI at 10.7 GHz only. For other land cover types, A_1 and A_0 were estimated using the general relationship with either FVC or monthly minimum MPDI at 10.7 GHz (see Table IV). The best estimators of A_1 and A_0 for each land cover on the basis of the R values were selected in bold within Table IV.

A_1 is highly correlated with FVC. For instance, in grassland and forest, the correlation coefficient R is 0.843 and 0.854, respectively, indicating that FVC is an effective predictor of A_1 in these land cover types. However, in bare soil, the correlation between A_1 and FVC is notably low, i.e., R = 0.026, whereas the correlation with the monthly minimum MPDI at 10.7 GHz is relatively higher, i.e., R = 0.286. A_1 is less sensitive to FVC and the monthly minimum MPDI at 10.7 GHz (see Fig. 7). In the bare soil area, A_1 can be regarded as a constant at about 1.00. In addition, A_1 generally increases with FVC in grassland, cropland, and forest.

A_0 is strongly correlated with FVC in grassland, cropland, and especially in forest with R = 0.615, whereas the correlation with the monthly minimum MPDI at 10.7 GHz is

TABLE IV

FITTING EQUATIONS OF A_1 AND A_0 PARAMETERS (IVS: INDEPENDENT VARIABLES; FVC: FRACTIONAL VEGETATION COVER; $MPDI^*_{10.7}$: MONTHLY MIN MPDI VALUES AT 10.7 GHZ; R: CORRELATION COEFFICIENT)

Parameters	IVs	Land cover types	Inversion models	R
A_1	FVC	Grassland	$\boldsymbol{A_1 = 69.04\times(FVC)^2-28.49\times FVC+5.67}$	0.843
		Cropland	$A_1 = 12.41\times(FVC)^2+7.73\times FVC+3.32$	0.519
		Forest	$\boldsymbol{A_1 = 119.46\times(FVC)^2-29.63\times FVC+2.02}$	0.854
		Bare soil	**1.00**	/
		Others	$A_1 = 28.68\times(FVC)^2+0.18*FVC+2.21$	0.594
	$MPDI^*_{10.7}$	Grassland	$A_1 = 18109\times (MPDI^*_{10.7})^2 - 1266.5\times MPDI^*_{10.7}+24.76$	0.749
		Cropland	$\boldsymbol{A_1 = 0.0055\times (MPDI^*_{10.7})^{-1.58}}$	0.740
		Forest	$A_1 = 9E\text{-}06\times (MPDI^*_{10.7})^{-2.63}$	0.579
		Bare soil	$A_1 = -16.91\times MPDI^*_{10.7}+1.80$	0.286
		Others	$\boldsymbol{A_1 = 0.0052\times (MPDI^*_{10.7})^{-1.52}}$	0.640
A_0	FVC	**Grassland**	$\boldsymbol{A_0 = -1.05\times(FVC)^2+0.80\times FVC+0.004}$	0.429
		Cropland	$\boldsymbol{A_0 = -0.90\times(FVC)^2+0.50\times FVC+0.068}$	0.460
		Forest	$\boldsymbol{A_0 = -0.97\times(FVC)^2+0.49\times FVC+0.024}$	0.615
		Bare soil	**0.007**	/
		Others	$\boldsymbol{A_0 = -1.03\times(FVC)^2+0.68\times FVC+0.040}$	0.406
	$MPDI^*_{10.7}$	Grassland	$A_0 = -0.53\times MPDI^*_{10.7}+0.10$	0.041
		Cropland	$A_0 = -1.33\times MPDI^*_{10.7}+0.11$	0.082
		Forest	$A_0 = 4.74\times MPDI^*_{10.7}+0.01$	0.188
		Bare soil	$A_0 = -3.40\times MPDI^*_{10.7}+0.13$	0.608
		Others	$A_0 = -2.04\times MPDI^*_{10.7}+0.13$	0.209

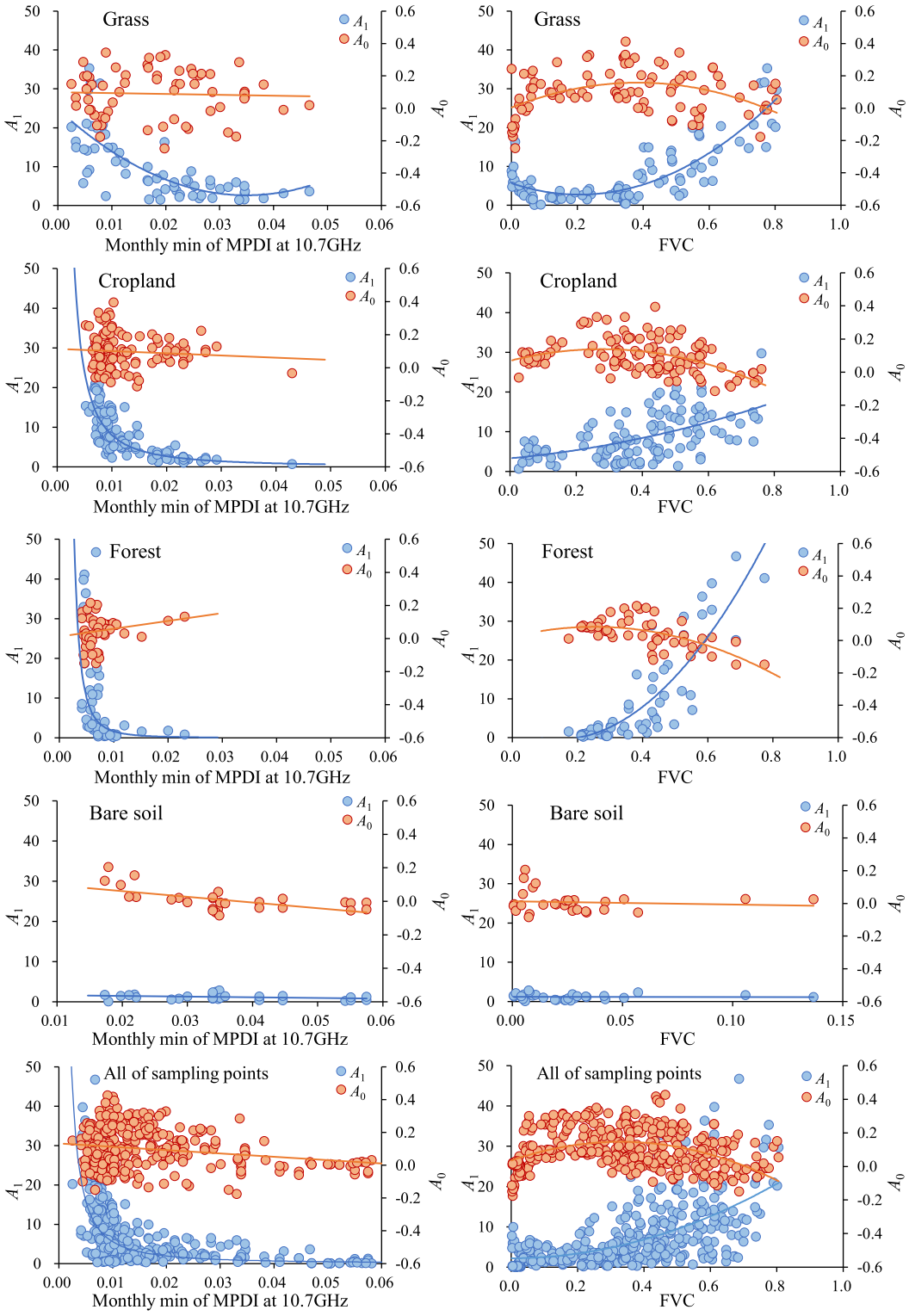

Fig. 7. Scatter plots between: (left) A_1 (or A_0) values and the monthly minimum of MPDI at 10.7-GHz data and (right) FVC.

generally lower. For instance, in the grassland, the correlation coefficient is $R = 0.041$, indicating a very weak relationship between A_0 and MPDI. This suggests that FVC is a better predictor of A_0. A_0 retrieval models generally decrease with FVC according to a negative quadratic relationship.

Overall, FVC is a better predictor of A_1 and A_0 than the monthly minimum MPDI at 10.7 GHz, especially in grassland and forest. The choice of the best relationship to estimate A_1 and A_0 also depends on the land cover. These findings reflect the complex relationships between SM and land cover, MDPI

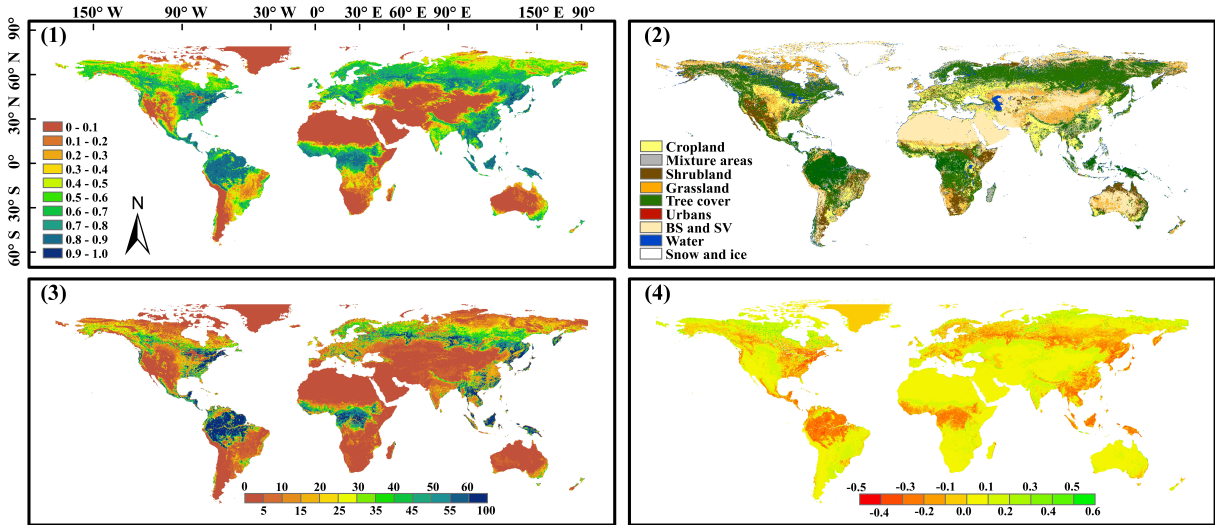

Fig. 8. Global distribution of (1) FVC, (2) main land cover, (3) A_1, and (4) A_0 in August 2010.

and FVC, which is a critical element in the retrieval of global SM.

2) Global-Scale Monthly A_0 and A_1 Retrievals: Monthly A_1 and A_0 were estimated globally from 2002 to 2011 using the relationships with FVC and MPDI (see Table IV). An example of the results for August 2010 is shown in Fig. 8. We found the global distribution of A_1, A_0, FVC, and land cover types was rather consistent. In Asia, northern America, and near the equator, A_0 values were higher, above 30. A_0 was lower, less than -0.1. In arid regions, such as in the Sahara in northern Africa, A_1 values were below 5, while A_0 values were scattered around -0.1.

A_1 is high in tropical rainforests in South America and Southeast Asia, reflecting high vegetation density and representing specific ecological conditions. Low A_1 values are found in deserts such as the Sahara and inland Australia, corresponding to areas of low vegetation density. Similarly, A_0 values are high in vegetation-rich regions such as tropical rainforests and some temperate areas, while low values are found in deserts and bare soil areas. Spatially, there is a clear correlation between A_1 (or A_0) and FVC. Typically, A_1 and A_0 values are high in areas of high vegetation density, indicating healthier and more active ecosystems. Areas of dense vegetation, such as tropical and temperate forests, stand out in both vegetation cover and A_1 (or A_0), reflecting favorable ecological and climatic conditions. Conversely, agricultural land, grasslands, deserts, and bare soil areas exhibit lower A_1 and A_0 values, indicating less favorable ecological conditions.

In summary, the A_1 and A_0 spatial distributions are strongly correlated with vegetation cover and land cover type. These relationships highlight the varying ecological health and functionality of different regions and provide important insights into global environmental and ecological change.

C. Improved Retrieval and Evaluation of the AMSR-E SM

1) Evaluation With In Situ SM Measurements: The improved AMSR-E, AMSR-E/NASA, AMSR-E/JAXA, and AMSR-E/LPRM retrievals were compared with in situ SM measurements from 612 sites across the six ISMN observation networks (see subset 2 in Table III), i.e., OZNET, SASMAS, MAQU, HYDROL-NET_PERUGIA, SNOTEL, and USCRN. One representative site was selected from each one of the six networks to visually demonstrate the performance of the improved algorithm, as shown in Fig. 9 for temporal evolution, Fig. 10 for scatterplots, and Table V for statistical metrics. These representative sites covered five land cover types, namely, irrigated cropland (Widgiewa site of OZNET), mixed forest/grassland (Cullingral site of SASMAS), grassland (NST_09 site of MAQU and HYDROL-NET_PERUGIA site), forest area (ARAPAHO_RIDGE site of SNOTEL), and rainfed cropland (Edinburg_17_NNE site of USCRN). The overall performance validated at 612 sites in the six networks was also given in Table V, while full validation information at 612 sites of six networks (OZNET, SASMAS, MAQU, HYDROL-NET-PERUGIA, USCRN, and SNOTEL) can be found in Table VIII in the Supplementary Material.

The land cover type at the Widgiewa site (OZNET) is irrigated farmland in Fig. 9(a). The measured SM value at this site is characterized by a sudden increase and then a gradual decrease over a certain period of time. This may be due to irrigation events. Compared with the AMSR-E/NASA SM products, the improved AMSR-E, AMSR-E/JAXA and AMSR-E/LPRM SM products show clear seasonal changes, with higher SM values around July and August and lower SM values around January and February. At the Widgiewa site (OZNET), compared with the AMSR-E/NASA, AMSR-E/JAXA, and AMSR-E/LPRM SM products, the improved AMSR-E SM products are more consistent with the in situ measurements, and the sample points are closer to a 1:1 line in Fig. 10(a).

The Cullingral site (SASMAS) is located in a mixed forest and grassland area. At the Cullingral site (SASMAS), around July 1, 2007, the measured SM value reaches a peak value of 0.43 cm^3/cm^3. In other periods, the measured SM value is lower, less than 0.25 cm^3/cm^3. In addition to the

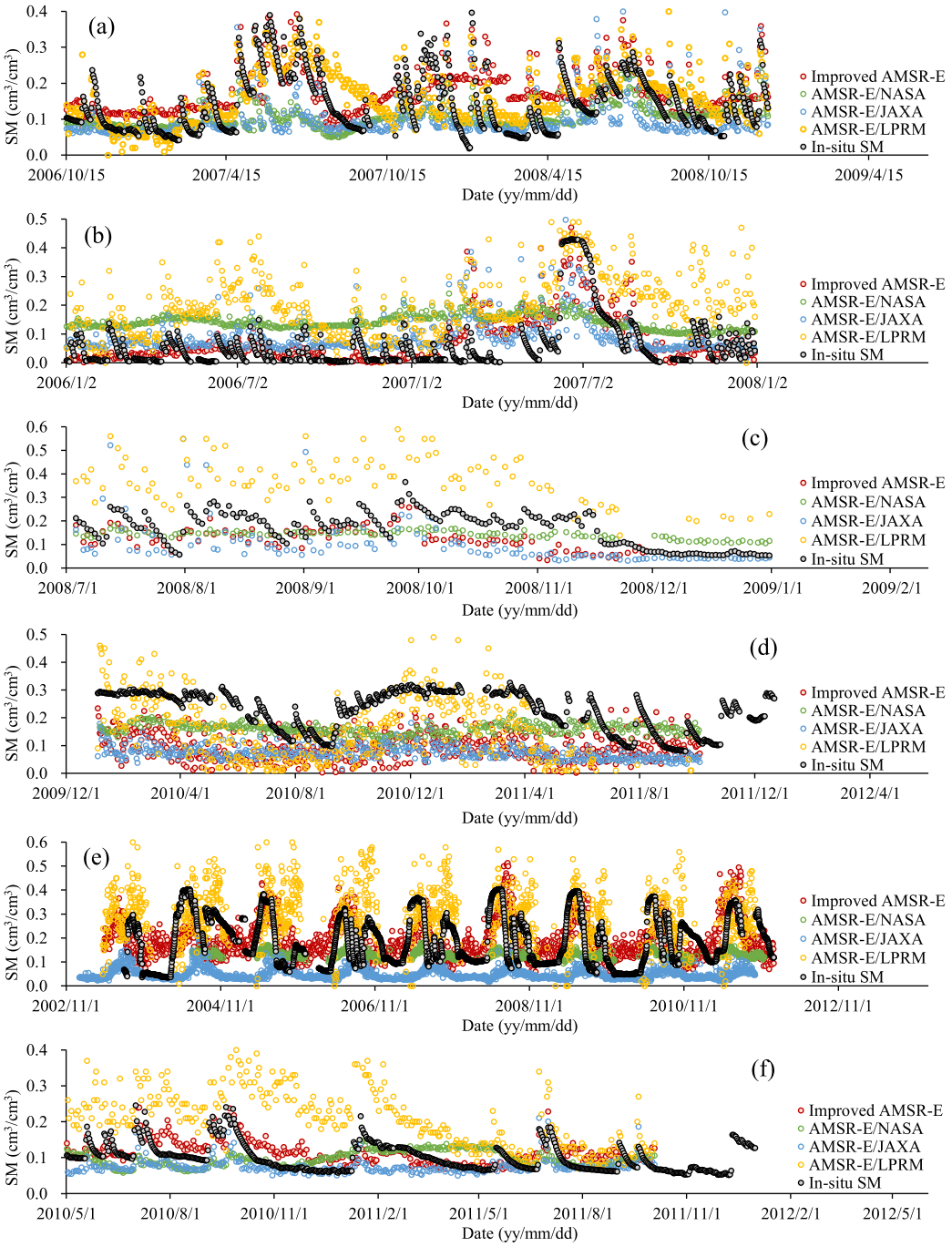

Fig. 9. Temporal evolutions of AMSR-E (improved, NASA, JAXA, and LPRM) SM products and in situ SM (cm^3/cm^3) measurements at the selected sites from the six networks for demonstration. (a) Widgiewa site of OZNET. (b) Cullingral site of SASMAS. (c) NST_09 site of Maqu. (d) HYDROL-NET_PERUGIA site. (e) ARAPAHO_RIDGE site of SNOTEL. (f) Edinburg_17_NNE site of USCRN.

AMSR-E/NASA SM product, the improved AMSR-E, AMSR-E/JAXA, and AMSR-E/LPRM SM products all record this significant SM change. The AMSR-E/NASA SM product values show little change over time, with SM values ranging from 0.09 to 0.23 cm^3/cm^3. In addition, the AMSR-E/LPRM SM product overestimates the measured SM value more seriously than the improved AMSR-E and AMSR-E/JAXA SM products at the Cullingral site (SASMAS). The improved AMSR-E SM product values are in best agreement with the in situ measurements, followed by AMSR-E/JAXA.

The NST_09 site (MAQU) is located in the grassland area. Most of the measured SM values at the NST_09 site (MAQU) were between 0.05 and 0.30 cm^3/cm^3. The AMSR-E/NASA SM product values show little variation over time, with SM values ranging from 0.10 to 0.20 cm^3/cm^3. In addition, there are many AMSR-E/LPRM SM values that overestimate the measured SM, while most of the improved AMSR-E and AMSR-E/JAXA values underestimate it. Compared with AMSR-E/NASA and AMSR-E/LPRM SM products, the improved AMSR-E and AMSR-E/JAXA SM products are

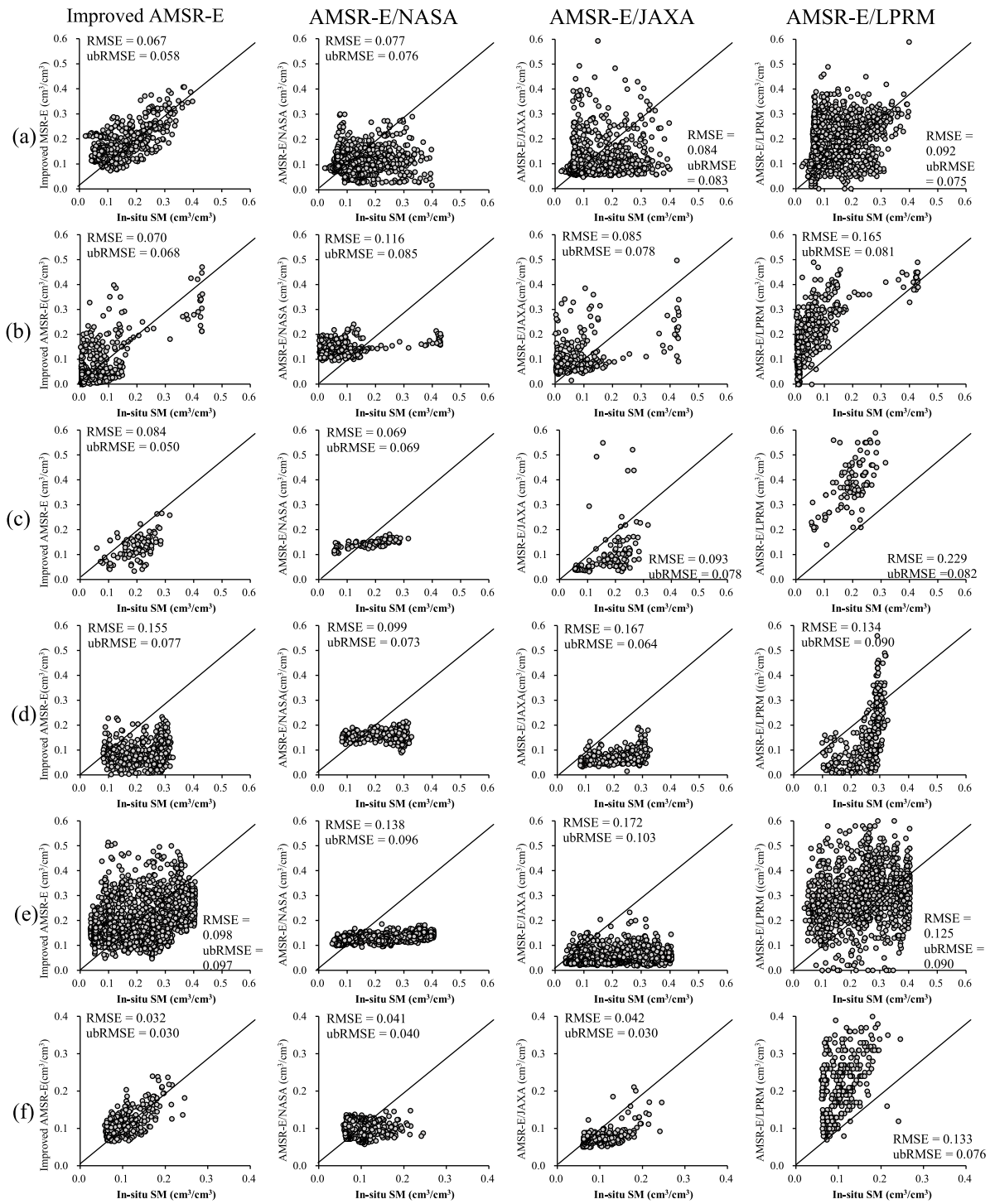

Fig. 10. Scatter plots with RMSE (cm^3/cm^3) and ubRMSE (cm^3/cm^3) between the AMSR-E SM products and in situ measurements at the selected sites from different networks for demonstration. (a) Widgiewa site of OZNET. (b) Cullingral site of SASMAS. (c) NST_09 site of Maqu. (d) HYDROL-NET_PERUGIA site. (e) ARAPAHO_RIDGE site of SNOTEL. (f) Edinburg_17_NNE site of USCRN.

more consistent with the in situ measurements at the NST_09 site (MAQU).

At the HYDROL-NET_PERUGIA network, most of the measured SM values are between 0.10 and 0.40 cm^3/cm^3 [56]. The improved SM products of AMSR-E, AMSR-E/NASA, AMSR-E/JAXA, and AMSR-E/LPRM all underestimate the SM at this site. AT the ARAPAHO_RIDGE site (SNOTEL), the measured SM shows clear seasonality, ranging from below 0.1 cm^3/cm^3 in January and February to over 0.35 cm^3/cm^3 in June. The AMSR-E/NASA and AMSR-E/JAXA SM show limited temporal variation (0.1–0.2 cm^3/cm^3), failing to capture the full seasonal cycle. The improved AMSR-E and AMSR-E/LPRM SM vary widely (0–0.5 and 0–0.6 cm^3/cm^3, respectively), and better track seasonal variation. However,

TABLE V
MAE (cm^3/cm^3), RMSE (cm^3/cm^3), ubRMSE (cm^3/cm^3), BIAS (cm^3/cm^3), AND R VALUES OF AMSR-E SM PRODUCTS AGAINST IN SITU SM MEASUREMENTS

Ob. Networks (Site: Land cover type)	Metrics	Improved AMSR-E	NASA	JAXA	LPRM
OZNET (Widgiewa: Irrigated cropland)	MAE	0.055	0.057	0.059	0.070
	RMSE	0.067	0.077	0.084	0.092
	Bias	0.034	-0.011	-0.014	0.053
	R	0.689	0.305	0.376	0.580
	ubRMSE	0.058	0.076	0.083	0.075
SASMAS (Cullingral: Mixing of forest/grass)	MAE	0.048	0.105	0.064	0.146
	RMSE	0.070	0.116	0.085	0.165
	Bias	0.015	0.080	0.032	0.144
	R	0.704	0.293	0.517	0.675
	ubRMSE	0.068	0.085	0.078	0.081
MAQU (NST_09: Grass)	MAE	0.073	0.061	0.070	0.214
	RMSE	0.084	0.069	0.093	0.229
	Bias	-0.068	-0.001	-0.051	0.214
	R	0.536	0.710	0.455	0.559
	ubRMSE	0.050	0.069	0.078	0.082
HYDROL-NET_PERUGIA (Grass)	MAE	0.139	0.086	0.154	0.115
	RMSE	0.155	0.099	0.167	0.134
	Bias	-0.134	-0.068	-0.154	-0.099
	R	0.210	0.047	0.425	0.706
	ubRMSE	0.077	0.073	0.064	0.090
SNOTEL (ARAPAHO_RIDGE: Forest)	MAE	0.093	0.114	0.138	0.117
	RMSE	0.098	0.138	0.172	0.125
	Bias	0.008	-0.099	-0.137	0.065
	R	0.329	0.298	0.198	0.227
	ubRMSE	0.097	0.096	0.103	0.129
USCRN (Edinburg_17_NNE: Rainfed cropland)	MAE	0.026	0.031	0.032	0.110
	RMSE	0.032	0.041	0.042	0.133
	Bias	0.011	-0.007	-0.029	0.109
	R	0.630	0.125	0.587	0.496
	ubRMSE	0.030	0.040	0.030	0.076
Average of all 612 sites in subset 2 of Table III	MAE	0.098	0.100	0.120	0.164
	RMSE	0.116	0.117	0.142	0.193
	Bias	-0.022	-0.041	-0.092	0.112
	R	0.292	0.235	0.144	0.313
	ubRMSE	0.086	0.080	0.088	0.117

the AMSR-E/LPRM product often overestimates the measured SM value in June each year. At both the HYDROL-NET_PERUGIA and ARAPAHO_RIDGE (SNOTEL) sites, there are large differences between the four SM products and the measured SM values. One of the reasons for this may be that both the HYDROL-NET_PERUGIA and SNOTEL networks were represented by only a single in situ site in our validation dataset. As a result, the evaluation reflects temporal agreement in Fig. 9(d) and (e) at a point scale, without the benefit of spatial averaging across multiple sites. This inherently increasing uncertainty and limits the representatives of the error statistics. Another may be the strong surface heterogeneity [57]. The HYDROL-NET_PERUGIA site features highly variable vegetation cover across the AMSR-E footprint, and the SNOTEL site (ARAPAHO_RIDGE) is located in complex mountainous terrain, where topography, forest density, and snow/freeze conditions vary significantly within a 25-km pixel [58], [59], [60]. These mismatches between the point-scale ground measurements and the satellite-scale retrieval likely contributed to the degraded performance.

The land cover at the Edinburg_17_NNE site (USCRN) is rainfed cropland. The range of in situ SM measurements at this site is 0.05–0.25 cm^3/cm^3. The SM ranges of the improved AMSR-E, AMSR-E/NASA, AMSR-E/JAXA, and AMSR-E/LPRM products are 0.05–0.25, 0.05–0.15, 0.05–0.22, and 0.05–0.40 cm^3/cm^3, respectively. The AMSR-E/NASA SM product has the smallest range, while the AMSR-E/LPRM SM product overestimates the measured SM values more often. AMSR-E/JAXA shows a larger underestimation of the measured SM value. The improved AMSR-E/NASA is more consistent with the SM, and the sample points are closer to the 1:1 line.

The evaluation metrics defined [see (15)–(19)] in Section III were also applied to the same set of in situ measurements (see Table V).

The improved AMSR-E SM was in better agreement with the in situ measurements at the sites Widgiewa, Cullingral, ARAPAHO_RIDGE, and Edinburg_17_NNE sites. The improved AMSR-E SM gave the lowest MAE, RMSE, and ubRMSE values at the Edinburg_17_NNE site, namely, 0.026, 0.032, and 0.030 cm^3/cm^3, respectively. The correlation coefficient of the improved AMSR-E SM was the highest at Cullingral, i.e., 0.704. The AMSR-E/NASA SM product at the NST_09 site had the smallest Bias, i.e., −0.001 cm^3/cm^3, while the improved AMSR-E SM product gave the lowest ubRMSE of only 0.050 cm^3/cm^3. The values of the improved AMSR-E, AMSR-E/NASA, AMSR-E/JAXA, and AMSR-E/LPRM SM products from HYDROL-NET_PERUGIA observation network sites were significantly different from the measured SM data, especially the AMSR-E/JAXA SM products.

Overall, the improved AMSR-E SM product values had a wider dynamic range, better reflected the annual and seasonal changes of SM, and were more consistent with the measured SM values compared with the AMSR-E/NASA SM products.

2) Comparison of the Global Spatial Patterns Captured by the Improved AMSR-E With the AMSR-E/NASA, JAXA, and LPRM SM Products: The improved daily global AMSR-E SM product with a spatial grid resolution of 25 km from 2002 to 2011 was generated using the global monthly A_1 and A_0 estimations and the AMSR-E MPDI data. The monthly improved AMSR-E SM was compared with the AMSR-E/NASA SM products from 2002 to 2011 (see Fig. 11). In addition, the daily improved AMSR-E SM was compared with the AMSR-E/NASA, JAXA, and LPRM on August 1, 2010 (see Fig. 12).

The improved AMSR-E SM has a much wider range (i.e., 0–0.6 cm^3/cm^3) than the AMSR-E/NASA SM (see Fig. 11). Especially in some regions with high vegetation cover, such as Central Africa, North and South America and Northern Asia, Malaysia, the improved AMSR-E SM is higher than 0.3 cm^3/cm^3, while the AMSR-E/NASA SM is lower than 0.25 cm^3/cm^3. In addition, the improved AMSR-E SM has a larger seasonal variability, which is consistent with the spatial distribution of vegetation cover. In the Sahara Desert, which is extremely dry throughout the year, however, most of the SM values of the improved AMSR-E SM product from January to October 2010 are between 0.15 and 0.2 cm^3/cm^3, which may overestimate the true SM.

The AMSR-E/NASA SM product shows a rather homogeneous distribution with values predominantly clustered in the lower range (see Fig. 11). The limited sensitivity of this

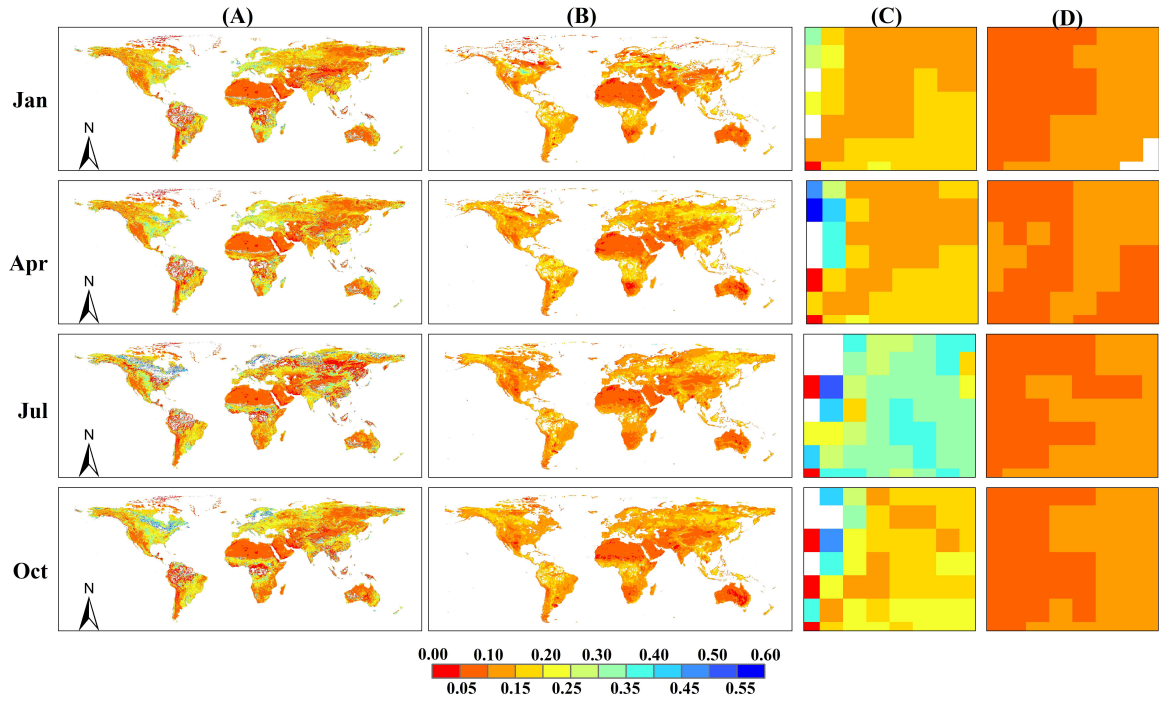

Fig. 11. Improved AMSR-E [(A) global and (C) Naqu, Tibetan Plateau] and AMSR-E/NASA [(B) global and (D) Naqu, Tibetan Plateau] SM (cm^3/cm^3) data products in January, April, July, and October, 2010.

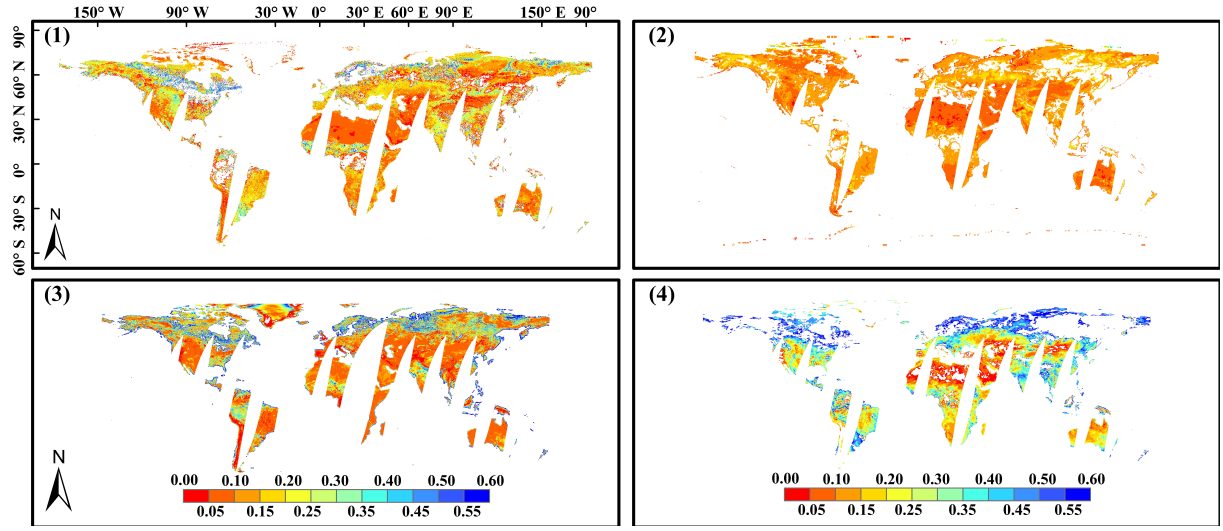

Fig. 12. Global distribution of four AMSR-E SM (cm^3/cm^3) products: the (1) improved AMSR-E, (2) AMSR-E/NASA, (3) AMSR-E/JAXA, and (4) AMSR-E/LPRM on August 1, 2010.

product to spatial variability is evident in its representation of arid and semi-arid regions, where it fails to capture finer moisture variations. In addition, it does not adequately reflect the higher SM levels expected in temperate regions, limiting its utility for detailed studies. The inability of the AMSR-E/NASA product to capture intra-annual and interannual SM variability further limits its effectiveness in applications such as agricultural drought monitoring and global climate research.

The improved AMSR-E, AMSR-E/JAXA, and AMSR-E/LPRM SM products perform better than AMSR-E/NASA, showing a wider range of SM values and better sensitivity to different moisture conditions (see Fig. 12). They capture the SM gradient from arid to humid regions more accurately, as seen in the transition from the arid Middle East to the wetter Southeast Asia. In addition, the improved AMSR-E shows a higher consistency with the spatial distribution of AMSR-E/JAXA SM product in identifying high SM areas. The improved AMSR-E and AMSR-E/JAXA SM product values are lower than AMSR-E/LPRM in forest areas with higher vegetation cover, such as North America and northern Asia. However, the AMSR-E/JAXA SM product shows many blank values in Africa and Europe.

In summary, the improved AMSR-E SM product outperforms the AMSR-E/NASA, AMSR-E/JAXA, and AMSR-E/LPRM products. It provides better agreement with in situ measurements (see Table V) and a more detailed representation of global SM variability (see Figs. 11 and 12). The improved AMSR-E product can capture more realistic spatial and

TABLE VI
KEY DIFFERENCES BETWEEN THIS STUDY AND XIE ET AL. [9] IN SM RETRIEVAL APPROACHES

Terms	Xie et al., 2019	This study
Study region	Tibetan Plateau	Global
Used data for vegetation	None	FVC
Temporal resolution	Monthly	Daily
A_0 and A_1 parameters	Empirical fitting using the MPDI and in-situ SM: $A_1 = 8$, $A_0 = 0.05$ or -0.15;	Global calibration of A_0 and A_1 using 192 in-situ sites (see Fig. 7 and Table IV).
SM retrieval method	Linear formulars: $\begin{cases} SM^t = -0.15 + 8 \times MPDI^t_{10.7} \ (t = 1, 2, 3, 4, 5, 6) \\ SM^t = 0.05 + 8 \times MPDI^t_{10.7} \ (t = 7, 8, 9) \end{cases}$ The $MPDI^t_{10.7}$ is the MPDI calculated at 10.7GHz from the AMSR-E BT data; the t is the month.	New nonlinear relationships linked to satellite FVC across different underlying surfaces (Eq.5~7, Table IV).
Evaluation sites	One network (CTP_SMTMN): 7 sites.	Six observation networks (OZNET, SASMAS, MAQU, HYDROL-NET_PERUGIA, SNOTEL, and USCRN): 612 sites.
Evaluation metric	RMSE = 0.065 cm^3/cm^3	RMSE = 0.032 cm^3/cm^3
Product output	None (analysis only)	GD_AMSR-E_SM: Global, 25 km, daily SM dataset (2002–2011).

*RTM: Radiative Transfer Model; FVC: Fractional Vegetation Coverage; MPDI: Microwave Polarization Difference Index; SM: Soil Moisture; BT: Brightness Temperature; RMSE: Root Mean Square Error.

seasonal variations in the global distribution of SM, particularly in transition zones and semi-arid regions such as the Tibetan Plateau, where other products tend to show overly smooth or limited variations. These improvement results in integrating recalibrated parameters and FVC and enabling more reliable SM retrievals across diverse climatic zones.

V. DISCUSSIONS

A. Improvement of This Study Compared With Xie et Al. [9], AMSR-E/JAXA, and AMSR-E/LPRM SM Retrieval Algorithms

This study utilized a satellite-based FVC and recalibrated A_0 and A_1 globally using in situ SM measurements from 192 sites, covering a wide range of vegetation types. Xie et al. [9] focused on the Tibetan Plateau and calibrated the vegetation-related A_0 and A_1 parameters using an empirical method based on MPDI and a limited number of in-site sites. While Xie et al. [9] identified the issue of the AMSR-E/NASA SM product in capturing intra-annual and interannual variability due to inaccurate estimation of A_0 and A_1, their work remained empirical and regional in nature. This study is completely different from Xie et al. [9], and the key differences are shown in Table VI.

The improved AMSR-E SM product developed in this study directly addresses a key limitation noted by Xie et al. [9], where the use of empirical parameter fitting and limited regional evaluation led to constrained dynamic range and weak sensitivity to intra-annual and interannual SM variations (see Table VI). In contrast, our study introduces a global calibration of the A_0 and A_1 parameters using in situ measurements from 192 sites across different underlying surfaces. The A_0 and A_1 parameters are linked to the satellite-based GLASS FVC dataset, enabling a nonlinear and land cover-specific parameterization scheme. This physically based recalibration leads to a globally consistent retrieval algorithm that better reflects the real-world SM conditions across diverse landscapes. As a result, the new GD_AMSR_SM product achieves improved accuracy (RMSE = 0.032 cm^3/cm^3 versus 0.065 cm^3/cm^3 in [9]) and provides daily global SM estimates at 25-km resolution from 2002 to 2011, expanding the utility of AMSR-E data for climate, hydrological, and agricultural applications.

A key differentiating feature of this study compared with AMSR-E/JAXA and AMSR-E/LPRM is the explicit incorporation of satellite-derived FVC into the SM retrieval algorithm. Unlike AMSR-E/JAXA, which considers vegetation effects negligible at low vegetation water content, and AMSR-E/LPRM, which employs an internal analytical VOD approach based solely on MPDI (see Tables II and VI), our approach directly links vegetation transmittance parameters (A_0 and A_1) to FVC [31]. This physically based parameterization captures the dynamic impacts of vegetation on microwave emissions more accurately, enabling robust SM retrieval across diverse vegetation conditions. Moreover, the global recalibration of vegetation parameters using extensive in situ measurements (192 sites) further enhances the reliability and representativeness of our retrieval method. In contrast, AMSR-E/JAXA employs a complex LUT approach with surface roughness simulations, adding potential uncertainty, while AMSR-E/LPRM assumes simplified vegetation and temperature conditions, limiting its general applicability [13], [31]. By integrating satellite-based FVC, globally calibrated parameters, and nonlinear vegetation modeling, the improved AMSR-E algorithm can be considered as an alternative SM retrieval algorithm to existing AMSR-E/JAXA and AMSR-E/LPRM.

B. Differences Between the Improved AMSR-E and the ESA-CCI SM Reference in Different Land Cover Types

To discuss how surface heterogeneity and vegetation cover influence the performance of the improved AMSR-E product, we utilized the combined datasets of ESA-CCI SM data (Version 7.1) as a reference to assess the improved AMSR-E SM product. The combined ESA-CCI SM dataset is a long-term (1978~2020), daily, and 0.25 spatial grid resolution global SM dataset, which combines multiple satellite passive and active microwave SM products through a triple collection analysis (TCA)-based algorithm [61], [62]. The combined ESA-CCI SM product is widely regarded as one of the benchmark datasets for evaluating satellite-based SM retrievals [63]. We calculated the global RMSE values between the improved AMSR-E and combined ESA-CCI SM datasets over the period from 2002 to 2011 (see Fig. 14 in the Supplementary Material). Fig. 13 shows the histograms and CDFs of the global

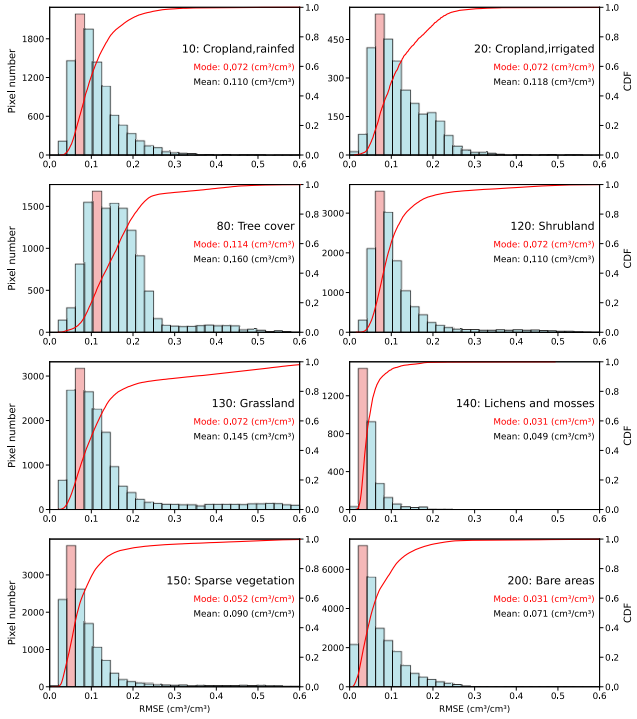

Fig. 13. Histograms and CDFs of the calculated RMSE (cm^3/cm^3) between the improved AMSR-E and ESA-CCI SM products from 2002 to 2011 across eight land cover types [rainfed cropland, irrigated cropland, tree cover, shrubland, grassland, lichens and mosses, sparse vegetation, and bare areas from the ESA-CCI Land Cover map, 2015 (see Fig. 1)].

RMSE map across eight land cover types (rainfed cropland, irrigated cropland, tree cover, shrubland, grassland, lichens and mosses, sparse vegetation, and bare areas from the ESA-CCI Land Cover map). In addition, we conducted the histograms and CDFs of the global RMSE map in different climate zones (Köppen-Geiger climate classification map) in Fig. 14 of the Supplementary Material [64].

In the sparse vegetation (150), lichens and mosses (140), and bare areas (200), the lowest errors were exhibited with both mode and mean RMSE values below 0.052 and 0.09 cm^3/cm^3. These surfaces typically have minimal vegetation water content, allowing more accurate microwave penetration and surface emission retrievals [65], [66]. In contrast, in densely vegetated areas such as the tree cover (80) and grassland (130), the RMSE values were significantly higher with the 0.114- and 0.072-cm^3/cm^3 mode value of RMSE. This is likely due to canopy-induced scattering and attenuation, which complicate SM signal retrieval in forested regions [58], [67]. Interestingly, in cropland areas including both rainfed and irrigated, there is similar performance (the mode RMSE value is 0.072 cm^3/cm^3), possibly benefiting from predictable surface structures and seasonal cycles. But, the mean RMSE values in irrigated cropland (0.118 cm^3/cm^3) are little higher in rainfed cropland (0.110 cm^3/cm^3), indicating that irrigation activities introduce additional spatial and temporal heterogeneity in SM conditions [68].

Overall, these results confirm the effectiveness of the improved AMSR-E algorithm in reducing SM retrieval errors across major land surface types when compared with ESA-CCI references. The product shows strong performance in open and sparsely vegetated regions, which are favorable for microwave remote sensing. Moreover, the cross validation with in situ networks remains essential for quantifying algorithm robustness over space and time.

C. Limitations and Research Outlook

Despite the improvements achieved in this study, several limitations remain. In densely vegetated areas, the MPDI may show limited variability due to the attenuation [32]. The purpose of parameterizing A_0 and A_1 is to estimate the below-canopy microwave signal based on the relatively uniform above-canopy MPDI. Retrieving the spatially varying A_0 and A_1 values as a function of FVC enables the algorithm to provide a pixel-specific interpretation of the vegetation effects on the observed signal. This allows for more accurate SM retrieval even in regions where the observed MPDI shows little spatial variation. Future improvements may focus on enhancing the temporal dynamics of the SM retrieval by integrating the surface temperature, precipitation, and high-resolution meteorological observations as well as topographic features [67], [69], [70]. These inputs may help to further refine the parameterization and extend the application of the algorithm. Future research will enhance the algorithm's short-term responsiveness and broader applicability by incorporating additional dynamic auxiliary variables. Moreover, combining machine learning techniques, e.g., the long-short term model (LSTM) due to its ability to learn temporal patterns and retain relevant past information while filtering out noise, it will be potential to better capture long- and short-term SM dynamics [69], [70].

In addition, the improved AMSR-E SM product exhibits relatively higher RMSE in snow-covered, frozen, or high-altitude terrain (see Fig. 14 in the Supplementary Material). These regions are particularly challenging for microwave SM retrieval due to altered dielectric properties of frozen soils, persistent snow cover, and terrain-induced signal distortions [60], [71]. The absence of winter-season and elevation-dependent validation may limit the algorithm's applicability in such environments. Future work will incorporate performance assessments during snow/freeze periods and across varying elevation gradients, using high-resolution elevation models and snow/freeze masks (e.g., MODIS snow products) to quantify associated uncertainties. Moreover, region-specific adjustments or mask-based filtering may be required to improve retrieval robustness in high-latitude and mountainous areas.

The improved AMSR-E algorithm will be extended to other satellite missions with similar sensor characteristics, such as AMSR-2 and the FY-3 series. This extension would enable the generation of longer term, temporally continuous, and spatially comprehensive SM datasets by bridging multiple satellite missions. However, differences in sensor calibration, radiometric accuracy, and observation geometry between AMSR-E, AMSR-2, and FY-3/MWRI should be considered and may introduce inconsistencies in parameter transfer and retrieval

accuracy [16]. To address these issues, intersensor harmonization and mission-specific recalibration of key parameters are necessary prior to operational implementation. In addition, the establishment and maintenance of extensive ground-based observation networks are essential to provide the data needed to calibrate and validate satellite-based SM products. Collaborative efforts between researchers, governmental agencies, and international organizations can help to expand these networks and ensure the availability of high-quality in situ data [54], [55].

VI. Conclusion

AMSR-E/NASA SM product values from 2002 to 2011 have a small dynamic range of variation and cannot capture the characteristics of interannual and seasonal changes in SM. In this study, the AMSR-E SM retrieval algorithm was improved to overcome these problems. An improved global AMSR-E SM product from 2002 to 2011 was generated. The main conclusions are as follows.

The spatial and temporal distribution of the AMSR-E/NASA, AMSE-E/JAXA and AMSR-E/LPRM SM products are significantly different. In particular, AMSR-E/NASA SM product values have small temporal and spatial variations and narrow interannual and interannual dynamic ranges, which can hardly reflect the characteristics of interannual and seasonal changes of SM. The improved AMSR-E SM product demonstrated a significantly wider dynamic range and stronger responsiveness to seasonal, annual, and interannual variations of the SM (see Figs. 9, 11, and 12).

Globally, A_1 and A_0 parameter values in the improved AMSR-E SM retrieval algorithms [(12)–(14)] are not constant, but change with vegetation cover, and there is a clear nonlinear correlation between them and FVC. A_1 and A_0 vary from 0 to 35 and from −0.2 to 0.4, respectively. Compared with the AMSR-E/NASA SM, the improved AMSR-E SM has a wider spatial–temporal range and is more consistent with the spatial distribution of vegetation cover.

The improved AMSR-E, AMSR-E/NASA, AMSR-E/JAXA, and AMSR-E/LPRM SM products were evaluated against the in situ SM measurements of six observation networks. The results showed that the improved AMSR-E had better performance and agreement with the in situ SM measurements with the lowest MAE (0.026 cm^3/cm^3), RMSE (0.032 cm^3/cm^3), and ubRMSE (0.030 cm^3/cm^3) and the highest correlation coefficient (0.704).

In conclusion, this study extends the development of passive microwave SM retrieval algorithms. The improved AMSR-E SM product offers a valuable tool for a wide range of applications, including drought monitoring, water resource management, climate diagnostics, and Earth system modeling. Its enhanced accuracy and consistency with in situ SM measurements strengthen its potential for use in both research and operational settings.

VII. Declaration of Competing Interest

All authors confirm no known competing financial interests or personal relationships that could have influenced the work reported in this article.

Acknowledgment

The authors express appreciation to all the organizations and teams contributing to global-scale Advanced Microwave Scanning Radiometer-Earth Observing System (AMSR-E)/National Aeronautics and Space Administration (NASA), AMSR-E/Japan Aerospace Exploration Agency (JAXA), AMSR-E/Land Parameter Retrieval Model (LPRM) soil moisture (SM) products, Global Land Surface Satellite (GLASS) fractional vegetation cover (FVC) data, and the in situ SM measurement data of the International Soil Moisture Network (ISMN) database service and China Scholarship Council are gratefully acknowledged.

References

[1] C. Song and L. Jia, "A method for downscaling FengYun-3B soil moisture based on apparent thermal inertia," *Remote Sens.*, vol. 8, no. 9, p. 703, Aug. 2016, doi: 10.3390/rs8090703.

[2] X. Qiuxia, J. Li, C. Qiting, Y. Yanmin, and M. Menenti, "Evaluation of microwave remote sensing soil moisture products in farming-pastoral area of shandian river basin," *Nat. Remote Sens. Bull.*, vol. 25, no. 4, pp. 974–989, 2021, doi: 10.11834/jrs.20219491.

[3] G. P. Petropoulos, G. Ireland, and B. Barrett, "Surface soil moisture retrievals from remote sensing: Current status, products & future trends," *Phys. Chem. Earth, A/B/C*, vols. 83–84, pp. 36–56, Mar. 2015, doi: 10.1016/j.pce.2015.02.009.

[4] J. Zhang et al., "Advances in estimation methods of vegetation water content based on optical remote sensing techniques," *Sci. China Technol. Sci.*, vol. 53, no. 5, pp. 1159–1167, May 2010, doi: 10.1007/s11431-010-0131-3.

[5] J. Shi et al., "Progresses on microwave remote sensing of land surface parameters," *Sci. China Earth Sci.*, vol. 55, no. 7, pp. 1052–1078, Jul. 2012, doi: 10.1007/s11430-012-4444-x.

[6] S. Nichols, "Review and evaluation of remote sensing methods for soil-moisture estimation," *J. Photon. Energy*, vol. 2, no. 1, Jan. 2011, Art. no. 028001, doi: 10.1117/1.3534910.

[7] J. Muñoz-Sabater, A. A. Bitar, and L. Brocca, "Soil moisture retrievals based on active and passive microwave data: State-of-the-art and operational applications," in *Satellite Soil Moisture Retrieval*, 2016, pp. 351–378.

[8] Q. Xie et al., "Evaluation of remote sensing soil moisture data products with a new approach to analyse footprint mismatch with in-situ measurements," *Int. J. Digit. Earth*, vol. 17, no. 1, pp. 1–35, Dec. 2024, doi: 10.1080/17538947.2024.2437051.

[9] Q. Xie, M. Menenti, and L. Jia, "Improving the AMSR-E/NASA soil moisture data product using in-situ measurements from the Tibetan Plateau," *Remote Sens.*, vol. 11, no. 23, p. 2748, Nov. 2019, doi: 10.3390/rs11232748.

[10] C. L. Parkinson, "Aqua: An Earth-observing satellite mission to examine water and other climate variables," *IEEE Trans. Geosci. Remote Sens.*, vol. 41, no. 2, pp. 173–183, Feb. 2003, doi: 10.1109/TGRS.2002.808319.

[11] T. Kawanishi et al., "The advanced microwave scanning radiometer for the Earth Observing System (AMSR-E), NASDA's contribution to the EOS for global energy and water cycle studies," *IEEE Trans. Geosci. Remote Sens.*, vol. 41, no. 2, pp. 184–194, Feb. 2003, doi: 10.1109/TGRS.2002.808331.

[12] J. Du, J. S. Kimball, and L. A. Jones, "Passive microwave remote sensing of soil moisture based on dynamic vegetation scattering properties for AMSR-E," *IEEE Trans. Geosci. Remote Sens.*, vol. 54, no. 1, pp. 597–608, Jan. 2016, doi: 10.1109/TGRS.2015.2462758.

[13] E. Njoku and S. Chan, "Vegetation and surface roughness effects on AMSR-E land observations," *Remote Sens. Environ.*, vol. 100, no. 2, pp. 190–199, Jan. 2006, doi: 10.1016/j.rse.2005.10.017.

[14] K. Imaoka, M. Kachi, M. Kasahara, N. Ito, K. Nakagawa, and T. Oki, "Instrument performance and calibration of AMSR-E and AMSR2," *Int. Arch. Photogramm., Remote Sens. Spatial Inf. Sci.*, vol. 38, pp. 13–16, Apr. 2010, doi: 10.15488/1434.

[15] J. Du et al., "Inter-calibration of satellite passive microwave land observations from AMSR-E and AMSR2 using overlapping FY3B-MWRI sensor measurements," *Remote Sens.*, vol. 6, no. 9, pp. 8594–8616, Sep. 2014, doi: 10.3390/rs6098594.

[16] J. Kolassa, R. H. Reichle, and C. S. Draper, "Merging active and passive microwave observations in soil moisture data assimilation," *Remote Sens. Environ.*, vol. 191, pp. 117–130, Mar. 2017, doi: 10.1016/j.rse.2017.01.015.

[17] R. van der Schalie et al., "The merging of radiative transfer based surface soil moisture data from SMOS and AMSR-E," *Remote Sens. Environ.*, vol. 189, pp. 180–193, Feb. 2017, doi: 10.1016/j.rse.2016.11.026.

[18] I. E. Mladenova et al., "Remote monitoring of soil moisture using passive microwave-based techniques—Theoretical basis and overview of selected algorithms for AMSR-E," *Remote Sens. Environ.*, vol. 144, pp. 197–213, Mar. 2014, doi: 10.1016/j.rse.2014.01.013.

[19] H. Fujii, T. Koike, and K. Imaoka, "Improvement of the AMSR-E algorithm for soil moisture estimation by introducing a fractional vegetation coverage dataset derived from MODIS data," *J. Remote Sens. Soc. Jpn.*, vol. 29, no. 1, pp. 282–292, 2009.

[20] P. W. Gaiser et al., "The WindSat spaceborne polarimetric microwave radiometer: Sensor description and early orbit performance," *IEEE Trans. Geosci. Remote Sens.*, vol. 42, no. 11, pp. 2347–2361, Nov. 2004, doi: 10.1109/TGRS.2004.836867.

[21] K. Imaoka et al., "Global change observation mission (GCOM) for monitoring carbon, water cycles, and climate change," *Proc. IEEE*, vol. 98, no. 5, pp. 717–734, May 2010, doi: 10.1109/JPROC.2009.2036869.

[22] H. Yang et al., "The FengYun-3 microwave radiation imager on-orbit verification," *IEEE Trans. Geosci. Remote Sens.*, vol. 49, no. 11, pp. 4552–4560, Nov. 2011, doi: 10.1109/TGRS.2011.2148200.

[23] H. M. J. P. Barre, B. Duesmann, and Y. H. Kerr, "SMOS: The mission and the system," *IEEE Trans. Geosci. Remote Sens.*, vol. 46, no. 3, pp. 587–593, Mar. 2008, doi: 10.1109/TGRS.2008.916264.

[24] D. Entekhabi et al., "The soil moisture active passive (SMAP) mission," *Proc. IEEE*, vol. 98, no. 5, pp. 704–716, May 2010, doi: 10.1109/JPROC.2010.2043918.

[25] J. S. Theon, "The tropical rainfall measuring mission (TRMM)," *Adv. Space Res.*, vol. 14, no. 3, pp. 159–165, Mar. 1994, doi: 10.1016/0273-1177(94)90210-0.

[26] J. P. Hollinger, J. L. Peirce, and G. A. Poe, "SSM/I instrument evaluation," *IEEE Trans. Geosci. Remote Sens.*, vol. 28, no. 5, pp. 781–790, Sep. 1990, doi: 10.1109/36.58964.

[27] T. Pellarin, Y. H. Kerr, and J.-P. Wigneron, "Global simulation of brightness temperatures at 6.6 and 10.7 GHz over land based on SMMR data set analysis," *IEEE Trans. Geosci. Remote Sens.*, vol. 44, no. 9, pp. 2492–2505, Sep. 2006, doi: 10.1109/TGRS.2006.874139.

[28] Y. C. Tzeng and K. S. Chen, "Wind reconstruction from ERS-1 scatterometer data using neural network," in *Proc. IEEE Int. Geosci. Remote Sens. Symp. Proceedings. Remote Sens. Sci. Vis. Sustain. Develop.*, vol. 3, Apr. 1997, pp. 1208–1210, doi: 10.1109/IGARSS.1997.606399.

[29] J. Figa-Saldaña, J. J. W. Wilson, E. Attema, R. Gelsthorpe, M. R. Drinkwater, and A. Stoffelen, "The Advanced Scatterometer (ASCAT) on the meteorological operational (MetOp) platform: A follow on for European wind scatterometers," *Can. J. Remote Sens.*, vol. 28, no. 3, pp. 404–412, Jan. 2002, doi: 10.5589/m02-035.

[30] H. Lu et al., "Development of a soil moisture retrieval algorithm for spaceborne passive microwave radiometers and its application to AMSR-E and SSM/I," in *Proc. IEEE Int. Geosci. Remote Sens. Symp.*, 2007, pp. 1177–1180, doi: 10.1109/IGARSS.2007.4423014.

[31] M. Owe, R. de Jeu, and T. Holmes, "Multisensor historical climatology of satellite-derived global land surface moisture," *J. Geophys. Res., Earth Surf.*, vol. 113, no. F1, pp. 1–17, Mar. 2008, doi: 10.1029/2007jf000769.

[32] E. G. Njoku, T. J. Jackson, V. Lakshmi, T. K. Chan, and S. V. Nghiem, "Soil moisture retrieval from AMSR-E," *IEEE Trans. Geosci. Remote Sens.*, vol. 41, no. 2, pp. 215–229, Feb. 2003, doi: 10.1109/TGRS.2002.808243.

[33] Q. Liu, J. Du, J. Shi, and L. Jiang, "Analysis of spatial distribution and multi-year trend of the remotely sensed soil moisture on the Tibetan Plateau," *Sci. China Earth Sci.*, vol. 56, no. 12, pp. 2173–2185, Dec. 2013, doi: 10.1007/s11430-013-4700-8.

[34] Y. Chen, K. Yang, J. Qin, L. Zhao, W. Tang, and M. Han, "Evaluation of AMSR-E retrievals and GLDAS simulations against observations of a soil moisture network on the central Tibetan Plateau," *J. Geophys. Res., Atmos.*, vol. 118, no. 10, pp. 4466–4475, May 2013, doi: 10.1002/JGRD.50301.

[35] A. K. Sahoo, P. R. Houser, C. Ferguson, E. F. Wood, P. A. Dirmeyer, and M. Kafatos, "Evaluation of AMSR-E soil moisture results using the in-situ data over the little river experimental watershed, Georgia," *Remote Sens. Environ.*, vol. 112, no. 6, pp. 3142–3152, Jun. 2008, doi: 10.1016/j.rse.2008.03.007.

[36] M. Owe, R. de Jeu, and J. Walker, "A methodology for surface soil moisture and vegetation optical depth retrieval using the microwave polarization difference index," *IEEE Trans. Geosci. Remote Sens.*, vol. 39, no. 8, pp. 1643–1654, Aug. 2001, doi: 10.1109/36.942542.

[37] T. J. Jackson et al., "Validation of advanced microwave scanning radiometer soil moisture products," *IEEE Trans. Geosci. Remote Sens.*, vol. 48, no. 12, pp. 4256–4272, Dec. 2010, doi: 10.1109/TGRS.2010.2051035.

[38] J. Liu et al., "Evaluation of SMAP, SMOS-IC, FY3B, JAXA, and LPRM soil moisture products over the Qinghai–Tibet Plateau and its surrounding areas," *Remote Sens.*, vol. 11, no. 7, p. 792, Apr. 2019, doi: 10.3390/rs11070792.

[39] J. Zheng et al., "Assessment of 24 soil moisture datasets using a new in situ network in the Shandian River Basin of China," *Remote Sens. Environ.*, vol. 271, Mar. 2022, Art. no. 112891, doi: 10.1016/j.rse.2022.112891.

[40] C. Draper, R. Reichle, R. de Jeu, V. Naeimi, R. Parinussa, and W. Wagner, "Estimating root mean square errors in remotely sensed soil moisture over continental scale domains," *Remote Sens. Environ.*, vol. 137, pp. 288–298, Oct. 2013, doi: 10.1016/j.rse.2013.06.013.

[41] A. Al-Yaari et al., "Global-scale evaluation of two satellite-based passive microwave soil moisture datasets (SMOS and AMSR-E) with respect to land data assimilation system estimates," *Remote Sens. Environ.*, vol. 149, pp. 181–195, Jun. 2014, doi: 10.1016/j.rse.2014.04.006.

[42] J. Zeng, Z. Li, Q. Chen, H. Bi, J. Qiu, and P. Zou, "Evaluation of remotely sensed and reanalysis soil moisture products over the Tibetan Plateau using in-situ observations," *Remote Sens. Environ.*, vol. 163, pp. 91–110, Jun. 2015, doi: 10.1016/j.rse.2015.03.008.

[43] N. S. Chauhan, S. Miller, and P. Ardanuy, "Spaceborne soil moisture estimation at high resolution: A microwave-optical/IR synergistic approach," *Int. J. Remote Sens.*, vol. 24, no. 22, pp. 4599–4622, Jan. 2003, doi: 10.1080/0143116031000156837.

[44] J. Thomas, M. Gupta, P. K. Srivastava, D. K. Pandey, and R. Bindlish, "Development of high-resolution soil hydraulic parameters with use of Earth observations for enhancing root zone soil moisture product," *Remote Sens.*, vol. 15, no. 3, p. 706, Jan. 2023, doi: 10.3390/rs15030706.

[45] K. Jia et al., "Global land surface fractional vegetation cover estimation using general regression neural networks from MODIS surface reflectance," *IEEE Trans. Geosci. Remote Sens.*, vol. 53, no. 9, pp. 4787–4796, Sep. 2015, doi: 10.1109/TGRS.2015.2409563.

[46] K. Jia et al., "Validation of global land surface satellite (GLASS) fractional vegetation cover product from MODIS data in an agricultural region," *Remote Sens. Lett.*, vol. 9, no. 9, pp. 847–856, Sep. 2018, doi: 10.1080/2150704x.2018.1484958.

[47] L. Yang, K. Jia, S. Liang, J. Liu, and X. Wang, "Comparison of four machine learning methods for generating the GLASS fractional vegetation cover product from MODIS data," *Remote Sens.*, vol. 8, no. 8, p. 682, Aug. 2016, doi: 10.3390/rs8080682.

[48] H. Lu, T. Koike, T. Ohta, H. Fujii, and H. Tsutsui, "Improving the AMSR-E soil moisture algorithm of the university of Tokyo through field experiments and parameters optimization," in *Proc. IEEE Int. Geosci. Remote Sens. Symp.*, Feb. 2008, pp. 65–68, doi: 10.1109/IGARSS.2008.4778928.

[49] K. S. Chen, T.-D. Wu, L. Tsang, Q. Li, J. Shi, and A. K. Fung, "Emission of rough surfaces calculated by the integral equation method with comparison to three-dimensional moment method simulations," *IEEE Trans. Geosci. Remote Sens.*, vol. 41, no. 1, pp. 90–101, Jan. 2003, doi: 10.1109/TGRS.2002.807587.

[50] B. Wen, L. Tsang, D. P. Winebrenner, and A. Ishimaru, "Dense medium radiative transfer theory: Comparison with experiment and application to microwave remote sensing and polarimetry," *IEEE Trans. Geosci. Remote Sens.*, vol. 28, no. 1, pp. 46–59, Jan. 1990, doi: 10.1109/36.45744.

[51] M. Dobson, F. Ulaby, M. Hallikainen, and M. El-Rayes, "Microwave dielectric behavior of wet soil-part II: Dielectric mixing models," *IEEE Trans. Geosci. Remote Sens.*, vols. GE–23, no. 1, pp. 35–46, Jan. 1985, doi: 10.1109/TGRS.1985.289498.

[52] J. R. Wang and T. J. Schmugge, "An empirical model for the complex dielectric permittivity of soils as a function of water content," *IEEE Trans. Geosci. Remote Sens.*, vols. GE-18, no. 4, pp. 288–295, Oct. 1980, doi: 10.1109/TGRS.1980.350304.

[53] G. Petropoulos and J. McCalmont, "An operational in situ soil moisture & soil temperature monitoring network for west wales, U.K.: The WSMN network," *Sensors*, vol. 17, no. 7, p. 1481, Jun. 2017, doi: 10.3390/s17071481.
[54] W. A. Dorigo et al., "The international soil moisture network: A data hosting facility for global in situ soil moisture measurements," *Hydrol. Earth Syst. Sci.*, vol. 15, no. 5, pp. 1675–1698, May 2011, doi: 10.5194/hess-15-1675-2011.
[55] W. Dorigo et al., "The international soil moisture network: Serving Earth system science for over a decade," *Hydrol. Earth Syst. Sci.*, vol. 25, no. 11, pp. 5749–5804, Nov. 2021, doi: 10.5194/hess-25-5749-2021.
[56] A. Flammini, R. Morbidelli, C. Saltalippi, T. Picciafuoco, C. Corradini, and R. S. Govindaraju, "Reassessment of a semi-analytical field-scale infiltration model through experiments under natural rainfall events," *J. Hydrol.*, vol. 565, pp. 835–845, Oct. 2018, doi: 10.1016/j.jhydrol.2018.08.073.
[57] T. E. Ochsner et al., "State of the art in large-scale soil moisture monitoring," *Soil Sci. Soc. Amer. J.*, vol. 77, no. 6, pp. 1888–1919, Nov. 2013, doi: 10.2136/sssaj2013.03.0093.
[58] T. J. Jackson et al., "Validation of Soil Moisture and Ocean Salinity (SMOS) soil moisture over watershed networks in the U.S.," *IEEE Trans. Geosci. Remote Sens.*, vol. 50, no. 5, pp. 1530–1543, May 2012, doi: 10.1109/TGRS.2011.2168533.
[59] T. Hu, T. Zhao, K. Zhao, and J. Shi, "A continuous global record of near-surface soil freeze/thaw status from AMSR-E and AMSR2 data," *Int. J. Remote Sens.*, vol. 40, no. 18, pp. 6993–7016, Sep. 2019, doi: 10.1080/01431161.2019.1597307.
[60] C. Mätzler and A. Standley, "Technical note: Relief effects for passive microwave remote sensing," *Int. J. Remote Sens.*, vol. 21, no. 12, pp. 2403–2412, Jan. 2000, doi: 10.1080/01431160050030538.
[61] Y. Y. Liu et al., "Trend-preserving blending of passive and active microwave soil moisture retrievals," *Remote Sens. Environ.*, vol. 123, pp. 280–297, Aug. 2012, doi: 10.1016/j.rse.2012.03.014.
[62] A. Gruber, W. A. Dorigo, W. Crow, and W. Wagner, "Triple collocation-based merging of satellite soil moisture retrievals," *IEEE Trans. Geosci. Remote Sens.*, vol. 55, no. 12, pp. 6780–6792, Dec. 2017, doi: 10.1109/TGRS.2017.2734070.
[63] A. Gruber, T. Scanlon, R. van der Schalie, W. Wagner, and W. Dorigo, "Evolution of the ESA CCI soil moisture climate data records and their underlying merging methodology," *Earth Syst. Sci. Data*, vol. 11, no. 2, pp. 717–739, May 2019, doi: 10.5194/essd-11-717-2019.
[64] H. E. Beck, N. E. Zimmermann, T. R. McVicar, N. Vergopolan, A. Berg, and E. F. Wood, "Present and future Köppen–Geiger climate classification maps at 1-km resolution," *Sci. Data*, vol. 5, no. 1, Oct. 2018, Art. no. 180214, doi: 10.1038/sdata.2018.214.
[65] E. G. Njoku and J.-A. Kong, "Theory for passive microwave remote sensing of near-surface soil moisture," *J. Geophys. Res.*, vol. 82, no. 20, pp. 3108–3118, Jul. 1977, doi: 10.1029/jb082i020p03108.
[66] Y. Y. Liu et al., "Developing an improved soil moisture dataset by blending passive and active microwave satellite-based retrievals," *Hydrol. Earth Syst. Sci.*, vol. 15, no. 2, pp. 425–436, Feb. 2011, doi: 10.5194/hess-15-425-2011.
[67] D. Entekhabi, R. H. Reichle, R. D. Koster, and W. T. Crow, "Performance metrics for soil moisture retrievals and application requirements," *J. Hydrometeorol.*, vol. 11, no. 3, pp. 832–840, Jun. 2010, doi: 10.1175/2010jhm1223.1.
[68] P. M. Lawston, J. A. Santanello, and S. V. Kumar, "Irrigation signals detected from SMAP soil moisture retrievals," *Geophys. Res. Lett.*, vol. 44, no. 23, pp. 11860–11867, Dec. 2017, doi: 10.1002/2017gl075733.
[69] P. Yao, J. Shi, T. Zhao, H. Lu, and A. Al-Yaari, "Rebuilding long time series global soil moisture products using the neural network adopting the microwave vegetation index," *Remote Sens.*, vol. 9, no. 1, p. 35, Jan. 2017, doi: 10.3390/rs9010035.
[70] P. Yao and H. Lu, "A long term global daily soil moisture dataset derived from AMSR-E and AMSR2 (2002–2019)," *Nat. Tibetan Plateau Data Center*, vol. 2, pp. 1–16, May 2020.
[71] A. Rango, A. T. C. Chang, and J. L. Foster, "The utilization of spaceborne microwave radiometers for monitoring snowpack properties," *Hydrol. Res.*, vol. 10, no. 1, pp. 25–40, Feb. 1979, doi: 10.2166/nh.1979.0003.

Qiuxia Xie received the Ph.D. degree in cartography and geographic information systems from the Aerospace Information Research Institute, Chinese Academy of Sciences, Beijing, China, in 2021.

She is currently a Teacher with the School of Surveying and Geo-Informatics, Shandong Jianzhu University, Jinan, China. She has made active contributions to the development of remote sensing microwave soil moisture retrieval methodologies and multisource remote sensing data fusion for agriculture water resource management, global environmental change, and drought monitoring. Her research interests include the study of microwave remote sensing, soil water balance, hydrological modeling, and drought monitoring.

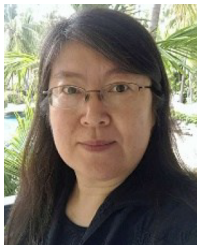

Li Jia (Member, IEEE) received the Ph.D. degree in environmental science from Wageningen University, Wageningen, The Netherlands, in 2004.

She is currently a Leading Scientist in Earth observation for terrestrial water cycle, water resource, and climate change with the Aerospace Information Research Institute, Chinese Academy of Sciences, Beijing, China. She is also a member of the Global Energy and Water Exchanges Program—Scientific Steering Group (GEWEX-SSG). Her research interests include the study of Earth observation and its applications in hydrometeorology, water resources, agriculture, and climate change.

Massimo Menenti received the Laurea degree in physics from the Università di Roma, Rome, Italy, in 1972, and the Dr.Sc. degree in environmental sciences from Delft University of Technology, Delft, The Netherlands, in 1984.

He has held senior research and faculty positions at Wageningen University, Wageningen, The Netherlands; the École Nationale Supérieure des Physique de Strasbourg (ENSPS), Strasbourg, France; the National Research Council of Italy, Rome; and Delft University of Technology. He is currently a Professor with the Institute of Tibetan Plateau Research, Chinese Academy of Sciences, Beijing, China; the National Key Laboratory of Remote Sensing and Digital Earth, Aerospace Information Research Institute, Chinese Academy of Sciences; and Delft University of Technology. He has made ground-breaking and early contributions to the development of remote sensing methodologies for water resource management, climate change studies, and land surface temperature retrieval. He has played a leading role in various international research collaborations, including projects with ESA, NASA, and European Union, focusing on Earth observation, climate change, and hydrological modeling. His research integrates multisource satellite observations with numerical models to improve environmental monitoring and prediction. His research interests include land surface processes, remote sensing of land–atmosphere interactions, surface energy balance modeling, and hydrological cycle analysis.

Prof. Menenti has served as an editor and a reviewer for multiple geoscience and remote sensing journals.

Qiting Chen received the Ph.D. degree in cartography and geographic information systems from the Aerospace Information Research Institute, Chinese Academy of Sciences, Beijing, China, in 2017.

She is currently an Assistant Researcher with the Aerospace Information Research Institute, Chinese Academy of Sciences. Her research interests include atmosphere–land surface interaction.